European Journal of Medicinal Chemistry Reports 14 (2025) 100276

Contents lists available at ScienceDirect

European Journal of Medicinal Chemistry Reports

journal homepage: www.editorialmanager.com/ejmcr/default.aspx

Reversing TGF-β1-induced fibrotic phenotype in human lung fibroblasts using a PROTAC tool derived from an indoline-based HDAC6 inhibitor

Ilaria Cursaro [a,1], Valerio Ciccone [b,1], Valeria Tudino [a], Chiara Papulino [c], Laura Scalvini [d], Sandra Donnini [b], Lucia Morbidelli [b], Luca Bini [b], Claudia Landi [b], Chiara Contri [e], Silvia Pasquini [e], Fabrizio Vincenzi [e], Katia Varani [e], Alessio Lodola [d], Marco Mor [d,f], Rosaria Benedetti [c,g], Lucia Altucci [c,g,h], Stefania Butini [a], Gabriele Carullo [a,*], Sandra Gemma [a,**], Giuseppe Campiani [a]

[a] Dipartimento di Biotecnologie, Chimica e Farmacia, Università degli Studi di Siena, Via Aldo Moro 2, 53100, Siena, Italy
[b] Dipartimento di Scienze della Vita, Università degli Studi di Siena, Via Aldo Moro 2, 53100, Siena, Italy
[c] Dipartimento di Medicina di Precisione, Università della Campania "Luigi Vanvitelli", Via de Crecchio 7, 80138, Naples, Italy
[d] Dipartimento di Scienze degli Alimenti e del Farmaco, Università di Parma, Parco Area delle scienze 27/A, Campus Universitario, 43124, Parma, Italy
[e] Dipartimento di Medicina Traslazionale, Università di Ferrara, Via Luigi Borsari 46, 44121, Ferrara, Italy
[f] Microbiome Research Hub, University of Parma, Parma, Italy
[g] Program of Medical Epigenetics, Vanvitelli Hospital, 80138, Naples, Italy
[h] Biogem Institute of Molecular and Genetic Biology, 83031, Ariano Irpino, Italy

ARTICLE INFO

Keywords:
HDAC6
PROTACs
Pulmonary fibrosis
Targeted protein degradation
Epigenetics

ABSTRACT

Idiopathic pulmonary fibrosis (IPF) is a progressive and debilitating interstitial lung disease characterized by limited therapeutic options, with only two FDA-approved palliative agents currently available. Given its poor prognosis and the high incidence of lung transplantation, there is a pressing need to develop innovative and effective therapeutics. Histone deacetylase 6 (HDAC6) has been identified as a key driver of fibrotic progression in IPF, and selective inhibitors of this isoform were able to revert the fibrotic phenotypes. Proteolysis targeting chimeras (PROTACs) are heterobifunctional molecules that can trigger the degradation of a specific target in cells, including HDAC6 enzyme. Therefore, the application of PROTAC technology may represent a novel therapeutic strategy for IPF. We showcase the design, synthesis, and biological evaluation of a library of first-in-class antifibrotic HDAC6-targeting PROTACs, incorporating our *in-house* inhibitor **1** as the HDAC6 ligand. Newly developed PROTACs **5a** and **5c** showed effective degradation of HDAC6 in A549 lung cells and IMR-90 lung fibroblasts. **5a** and **5c** exhibited significant antifibrotic effects against the TGF-β1 induced fibrotic phenotype on IMR-90 cells, a model that mimics IPF conditions. The generation of putative ternary complexes involving PROTAC molecules, the E3-ligase cereblon (CRBN) and the HDAC6 target protein was supported by molecular modelling techniques, including protein-protein docking and molecular dynamics simulations. Mechanistic investigations, based on pull-down experiments, confirmed that the newly synthetized compounds were able to reduce HDAC6 levels through a proteasome- and CRBN-dependent mechanism as confirmed by experiments with neddylation and proteasome inhibitors. This pioneering exploration of targeted protein degradation in IPF-like conditions provides compelling evidence of its therapeutic promise, paving the way for a broader application of PROTACs in treating rare diseases.

* Corresponding author.
** Corresponding author.
E-mail addresses: gabriele.carullo@unisi.it (G. Carullo), gemma@unisi.it (S. Gemma).
[1] these authors equally contributed.

https://doi.org/10.1016/j.ejmcr.2025.100276
Received 6 March 2025; Received in revised form 20 May 2025; Accepted 20 May 2025
Available online 21 May 2025

1. Introduction

Idiopathic pulmonary fibrosis (IPF) is the most prevalent form of pulmonary fibrosis, affecting approximately 3 million individuals globally [1]. While currently classified as a rare disease, this designation may soon be reconsidered due to its rising incidence and prevalence worldwide [2]. IPF is characterized by the replacement of normal lung parenchyma with fibrotic tissue, resulting in progressive stiffening of the lungs, declining pulmonary function, and chronic hypoxemia. By definition, the etiology of IPF is unknown; however, both genetic predispositions, such as mutations in *MUC5B*, and environmental factors, including aging, smoking, air pollution, and oxidative stress, are recognized as critical contributors to its pathogenesis [1]. Current understandings suggest that the fibrogenic process is driven by dysfunctional alveolar and airway epithelial response following repeated injuries [3,4]. Damaged alveolar epithelial cells (AECs) release a range of profibrotic cytokines and chemokines, with transforming growth factor β1 (TGF-β1) emerging as a central mediator [5]. TGF-β1 initiates a cascade of fibrotic events, including epithelial-mesenchymal transition (EMT), fibroblast proliferation and migration, and differentiation into myofibroblasts, ultimately leading to pathological extracellular matrix (ECM) deposition [4,6]. The current treatment options for IPF are limited to two FDA-approved drugs (pirfenidone-Esbriet® and nintedanib-Ofev®) which merely delay exacerbation of the disease with lung transplantation being last-resort measures. Altogether these latter highlight a critical unmet need for effective therapeutics [7]. The disruption of epigenetic homeostasis, driven by exposure to environmental risk factors and the aging process, is recognized as a pivotal factor in the development of IPF [8]. This dysregulation alters the epigenetic landscape of pulmonary fibroblasts, predisposing them to aberrant gene expression profiles that promote the initiation and progression of fibrotic pathways [8–10]. Inhibition of histone deacetylase (HDAC) activity, using pan- or isoform-selective HDAC inhibitors (HDACis), has shown efficacy in mitigating fibrosis in the heart, liver, and kidneys, highlighting HDAC as a promising therapeutic target for IPF [10–15]. Several studies have shown that HDAC6, a class IIb isoform with prevalent cytosolic localization, plays a key role during fibrogenesis by modulating several processes primarily through the deacetylation of its main non-histone substrate, α-tubulin. HDAC6 sustains the fibrotic response in lung tissues by modulating the TGF-β1- phosphoinositide 3-kinase-protein kinase B (TGF-β1-PI3K-AKT) and TGF-β1-mothers against decapentaplegic homolog 3 (SMAD3) signaling pathways [10,16,17]. Our immunohistochemistry experiments on three-dimensional organoids derived from airway basal cells of IPF patients underscored HDAC6 overexpression, corroborating previous reports which disclosed HDAC6 as the prevalent isoform expressed in IPF-AEC type II (AECII) but not in AECII of normal lungs [18,19]. Notably, the antifibrotic potential of both pan-HDACis and HDAC6is was explored in models of IPF and other fibrotic lung diseases [12,16,18,20]. Our research group has been actively engaged in the development of selective or multi-target HDACis as therapeutic agents for the treatment of cancers, infectious diseases, neurodegenerative and rare disorders [21–28]. In the context of IPF, we developed a library of indoline-derived selective HDAC6is, which demonstrated promising antifibrotic effects in *in vitro* and ex vivo models derived from IPF patient samples. These inhibitors effectively restored acetylated α-tubulin levels, inhibited EMT, and reversed key aspects of the IPF phenotype [18,29]. Featuring two independent catalytic domains (CDs) and a ubiquitin-binding zinc finger domain, HDAC6 is unique among the 11 isoforms. The pharmacophoric requirements for HDAC6 inhibition include a zinc-binding group that chelates the catalytic zinc ion, a linker that fits within the hydrophobic channel and a cap group that protrudes towards the solvent-exposed surface of the pocket [30]. In addition to its histone and non-histone deacetylase activity, it exerts several non-catalytic functions essential to cellular homeostasis [31].

Taking this into consideration, we decided to investigate the effect of the reversible abolition of catalytic and non-catalytic functions of HDAC6 in IPF-like conditions, exploiting a chemically induced targeted protein degradation (TPD) approach. Proteolysis targeting chimeras (PROTACs) are comprised of an E3 ligase ligand and a protein of interest (POI) ligand, tethered by a linker. The POI ligand drives target recruitment and allows the formation of an active E3 ligase-PROTAC-POI ternary complex. PROTACs act by hijacking the ubiquitin-proteasome system by inducing the polyubiquitination of the POI, flagging it for degradation (Fig. 1) [32]. PROTAC-mediated TPD is becoming a prominent strategy for degrading disease-causing proteins and expanding the druggable proteome for cancer treatment [33]. Valuable insights for designing HDAC6-targeting PROTACs are available in literature [34–38].

Yang et al. disclosed the potent nexturastat A-embedding HDAC6 degrader **NH2** (**2**, Fig. 1), which demonstrated effective reduction of HDAC6 levels in various cell lines, though it was primarily used as a reversible knock-down tool [39]. Additionally, vorinostat (SAHA)-based HDAC6-targeting PROTACs have shown significant promise as antiproliferative agents in myeloid leukemia cells [38].

Recently, TO-1187 was identified as a promising HDAC6 degrader, and a comprehensive proteomic assessment revealed a highly selective degradation profile, with HDAC6 as the only protein notably reduced [40]. Yet, the exploration of PROTACs as potential therapeutic tools for treating fibrosis remains relatively underdeveloped, with current research limited to kidney and liver fibrosis [41,42]. Building on PROTACs' success in cancer therapy, we strategically explored their pioneering application in IPF-like conditions. The indoline **1** (*h*HDAC6 IC_{50} = 41.9 nM, Fig. 1) was identified as a promising hit compound, displaying two-digit nanomolar potency on HDAC6 inhibition, low cytotoxicity, a favorable pharmacokinetic profile and a significant antifibrotic effect. Exploiting our in-house HDAC6 inhibitor **1** as a chemical handle, we designed and synthesized a small library of HDAC6-targeting PROTACs (**5a-d**, **23c** and **6**, Fig. 1 and Table 1), incorporating various linkers. Western blot analyses were conducted on A549 lung cancer cells and in IMR-90 fibroblasts to validate HDAC6 engagement (measured as increased acetylation of α-tubulin) and HDAC6 degradation. Furthermore, the reversion of fibrotic phenotype in TGF-β1-induced fibrosis on IMR-90 lung fibroblasts together with the proteasome- and CRBN-mediated mode of action were investigated.

2. Results and discussion

2.1. Structure-guided rational drug design

Our proprietary HDAC6 inhibitor **1** (Fig. 1), whose structure has been solved in *zf*HDAC6 (PDB id: 6V79), has proven effective in reversing the IPF phenotype both in organoids and human fibroblasts [18,29]. We selected it as the POI ligand for developing novel HDAC6-targeting PROTACs. To identify a suitable exit vector, structural analysis of the co-crystal complex of **1** within *zf*HDAC6 CD2 (PDB id: 6V79) was carried out. The indoline ring, functioning as the cap group, was found to be optimally exposed to the solvent and the benzo-fused ring was predicted as a favorable and synthetically accessible tethering site. An additional superposition of nexturastat A and **1** co-crystal structures in HDAC6 was performed to assess similarities in their binding mode. Accordingly, position 5 of the indoline ring of compound **1** was selected as the preferred exit vector and decorated with an amino moiety, yielding compound **3** (Fig. 1). Building on the insights gained from effective HDAC degraders, an amide bond was selected as the connecting unit for its chemical and metabolic stability, as well as synthetic accessibility. Cereblon (CRBN) and Von-Hippel Lindau (VHL) E3 ligases are among the most well-established target E3 ligases for PROTACs development. Pomalidomide (**4**, Fig. 1) was selected as the ligand for the design, given the higher expression of CRBN — its target E3 ligase — in lung tissues compared to the VHL E3 ligase, as reported on the Human Protein Atlas database [43]. Several linkers were

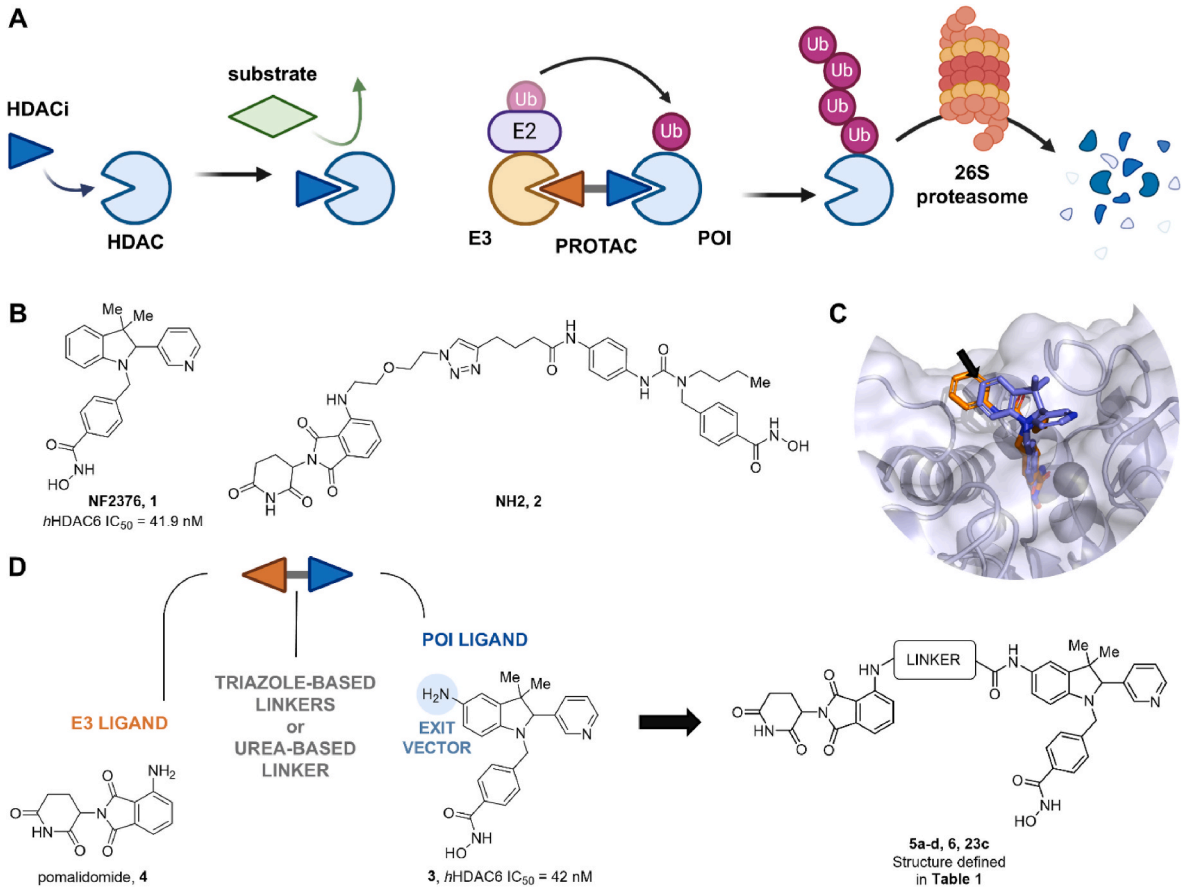

Fig. 1. **A**) Comparison of the mode of action of traditional inhibitors and PROTACs. **B**) Chemical structures of the antifibrotic HDAC6 inhibitor **1** and reported HDAC6 degrader **2**. **C**) Structural alignment of ligands in the X-ray structures of *zf*HDAC6 CD2 shown as light blue cartoon and bound to **1** (slate carbon atoms) and *zf*HDAC6 CD1 and CD2 in complex with Nexturastat A (bright orange carbon atoms) (PDB id: 6V79 and 5G0J). The black arrow indicates the selected exit vector on compound **1** for degrader design. **D**) Design strategy illustrating the integration of compound **1** into novel CRBN-recruiting HDAC6 degraders.

investigated, drawing inspiration from the chemical features of the linker embedded in NH2 (**2**, Fig. 1). Therefore, we devised a small selection of linkers presenting a triazole ring and a polyethyleneglycol-like alkyl chain to balance polarity and flexibility. PROTACs **5a-d** (Table 1) were designed to fine-tune the length and chemical composition of the linker to achieve optimal degradation efficacy. We also synthesized the "linkerless" PROTAC **6** (Table 1).

2.2. Chemistry

The synthesis of key intermediate **3** is reported in Scheme 1. Compound **7** was reacted with *p*-toluenesulfonyl acetone hydrazone—obtained by following the procedure described starting from commercially available reagents [18]—in presence of Cs_2CO_3 to yield the asymmetric ketone **8**. A Fischer protocol with 4-nitrophenylhydrazine and 12N HCl was applied, furnishing indolenine **9**, which was converted into the corresponding indoline **10** employing an *in situ* generated borane-acid complex as the reducing agent. Coupling of 4-bromomethyl benzoic acid **11** with *O*-THP-protected hydroxylamine afforded intermediate **12**, which was used to alkylate the indolinic nitrogen of **10**, furnishing compound **13**. The 5-nitro group of intermediate **13** was reduced to its corresponding aniline derivative **14** via an iron powder-mediated reaction. The target compound **3** was obtained by treating intermediate **14** with a methanolic solution of hydrogen chloride.

The synthesis of the alkyne-based synthons **18a,b** was performed according to Scheme 2.

Notably, ethyl 4-bromo butyrate (**15**) was simultaneously hydrolyzed and converted into its propargyl ether derivative **16** by treatment with propargyl alcohol under basic aqueous conditions. Carboxylic acid **16** was coupled with intermediate **14** in the presence of EDC-HCl as the condensing agent, HOBt and DMAP as additives and DIPEA as base, furnishing compound **18a**. Similarly, a HATU-mediated coupling of 6-heptynoic acid **17** with intermediate **14** furnished compound **18b**. Scheme 3 describes the synthesis of the azide-based synthons **22a-c** starting from the commercially available azide-bearing alkyl amines **18** and **19**, and **20**, which was prepared according to literature procedure [44]. Amines **18**–**20** were reacted with 4-fluorothalidomide and DIPEA at 80 °C, yielding intermediates **22a-c**.

The synthesis of PROTACs **5a-d** is reported in Scheme 4. The suitable azide-alkyne pairings were reacted in a copper-catalyzed cycloaddition in DMF, yielding desired intermediates. Specifically, **18a** was reacted with **22a-c** to furnish respectively **23a**, **23b** and **23d**. Analogously, when 18b was reacted wih **22a**, compound **23c** was obtained. An optimized *O*-THP deprotection protocol employing an aqueous solution of formic acid was applied to furnish the target compounds **5a-d**.

The linkerless PROTAC **6** was obtained as described in Scheme 5. Pomalidomide (**4**) was reacted with *p*-nitrophenyl chloroformate to furnish the activated carbamate **24**, which reacted with intermediate **14** under basic conditions to give compound **25**. Formic acid-mediated deprotection yielded compound **6**.

Table 1
Inhibitory activity of developed compounds toward *h*HDAC6, *h*HDAC1, *h*HDAC8 and *h*HDAC10 (as IC_{50}, nM).

Cpd	Structure	IC_{50} (nM)			
		*h*HDAC6	*h*HDAC1	*h*HDAC8	*h*HDAC10
5a	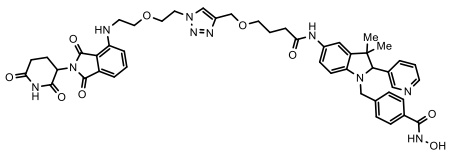	43 ± 3	162 ± 11	864 ± 51	2447 ± 168
5b	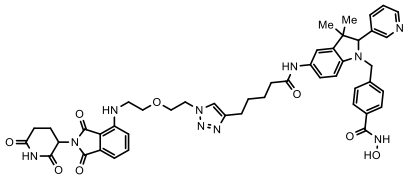	139 ± 8	1036 ± 74	3558 ± 218	>10000 (26 %)
5c	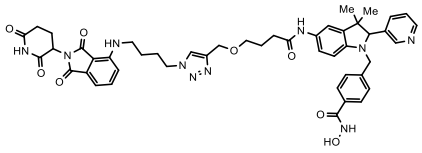	8.96 ± 0.61	287 ± 19	6817 ± 423	7079 ± 489
5d	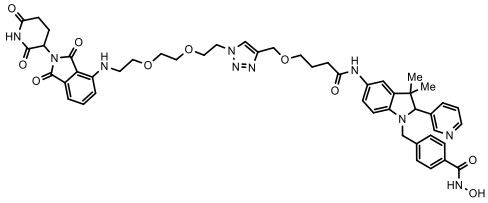	64 ± 4	74.7 ± 5.3	>10000 (15 %)	>10000 (40 %)
6	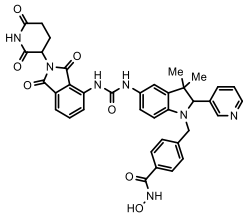	16.9 ± 1.2	653 ± 42	>10000 (41 %)	1327 ± 85
23c	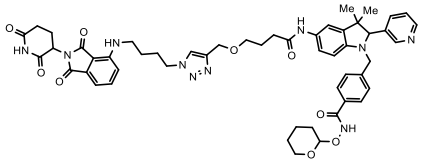	>10000 (9 %)	>10000 (12 %)	>10000 (36 %)	>10000 (2 %)
1		40.8 ± 1.51	5421 ± 268	NT[a]	2204 ± 198
3		41.9 ± 3.1	263 ± 17	1151 ± 88	1670 ± 104

Each value is the mean of at least three determinations; results are expressed with ±standard error of the mean (SEM); NT[a], not tested.

2.3. In vitro inhibitory activity against human HDAC6, HDAC1, HDAC10, HDAC8 and HDAC6 degradation evaluation in A549 lung cancer cells

The PROTACs **5a-d**, **23c** and **6** were first analyzed for their ability to inhibit HDAC6 and HDAC1, HDAC8, HDAC10 as primary off-targets (Table 1). **5a**, characterized by a bis(2-ethoxyethyl) spacer between the triazole moiety, showed an IC_{50} value of 43 nM on HDAC6, in line with the inhibitory activity of **1** and **3** (IC_{50} of 40.8 nM and 42 nM respectively, Table 1), when tested on HDAC6 in the same conditions. **5a** showed an improved inhibitory activity against HDAC1 and HDAC8 (IC_{50} = 462 and 864 nM, respectively) compared to the parent compound **1** ($IC_{50HDAC1}$ = 5421 nM and $IC_{50HDAC8}$ = 2204 nM). **5b**, analogue of **5a** bearing a poly-methylene chain on the POI ligand side, showed an interesting value of inhibition only in the case of HDAC6, with IC_{50} = 139 nM (Table 1). The inverted analogue **5c**, with the butyl chain on the pomalidomide side and same length of **5b**, resulted the most potent HDAC6 inhibitor of the series with an IC_{50} value of 8.96 nM and with a fair selectivity *vs* HDAC10, HDAC8 and HDAC1. The polyethyleneglycol-based analogue **5d** displayed no selectivity among HDAC6 and HDAC1 with IC_{50} values of 64 nM and 74.7 nM respectively (Table 1). The analogue **23c**, synthesized to confirm the necessity of a free hydroxamate group for enzyme inhibition and recruitment to induce degradation, did not exhibit any inhibitory activity against the four tested HDAC isoforms, as anticipated. Finally, the linkerless analogue **6**, which was constituted by pomalidomide and POI connected by only a urea

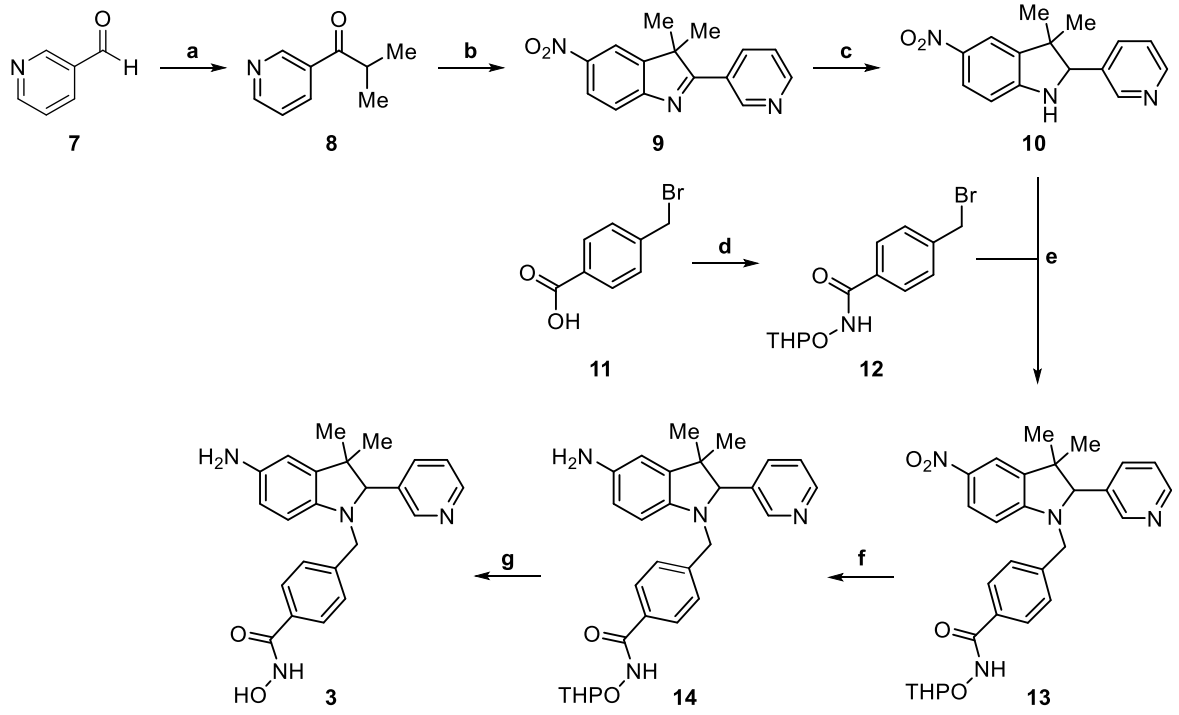

Scheme 1. Reagents and conditions: **a**) 3-pyridinecarboxaldehyde, Cs_2CO_3, dry 1,4-dioxane, 110 °C, 18 h, 59 %; **b**) 4-nitrophenylhydrazine, 12 N HCl, 70 °C, 18 h, 45 %; **c**) catecholborane 1.0 M in THF, TFA, 0 °C, 5 min, 99 %; **d**) *O*-(tetrahydro-2*H*-pyran-2-yl)hydroxylamine, EDC-HCl, dry DCM, dry DMF, rt, 16 h, 99 %; **e**) step 1. NaH, dry DMF, 0 °C, 1 h, step 2. **12**, 0 °C to rt, 18 h, 99 %; **f**) Fe, NH_4Cl, EtOH/H_2O, 78 °C, 3 h, 99 %; **g**) 1 N HCl in MeOH, MeOH, rt, 3 h, 24 %.

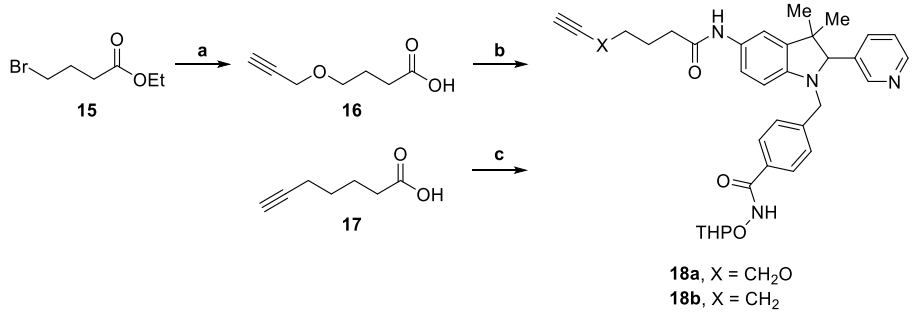

Scheme 2. Reagents and conditions: **a**) propargyl alcohol, TBAI, 10M NaOH, 50 °C, 18 h, 64 %; **b**) **14**, EDC-HCl, HOBt, DMAP, DIPEA, MeCN, rt, 20 h, 98 %; **c**) **14**, HATU, DIPEA, dry DMF, rt, 16 h, 77 %.

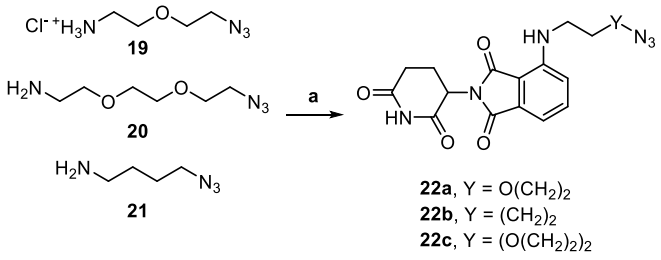

Scheme 3. Reagents and conditions: **a**) 4-fluoro-thalidomide, DIPEA, dry DMSO, 80 °C, 16 h, 34–45 %.

group, showed an IC_{50} value on HDAC6 of 16.9 nM (Table 1). The compounds did not show toxicity in the A549 cells at 1,5,10, 25 and 50 μM as shown in Fig. S1. We next analyzed the degradation efficiency of these new chemical entities in a well-established HDAC6 expressing cell model (i.e., A549 lung cancer cells). All the compounds were first screened at a concentration of 10 μM for 24 h of incubation in order to evaluate the levels of acetylated α-tubulin and HDAC6 degradation. As reported in Fig. 2A, **3** and **5d** were able to increase the levels of acetylated α-tubulin, together with the known compounds SAHA (used at 5 μM) and Tubastatin A (TubA, used at 10 μM). Moreover, at this concentration, it is possible to observe a promising HDAC6 degradation for compounds **5a**, **5b** and **5c**, with no significant activity in the case of **23c** and **6** (Fig. 2A). Predictably, pomalidomide (**4**) did not show any effects in modulating HDAC6 activity. These preliminary data prompted us to further investigate compounds **5a** and **5c**, since **5b** provided preliminary ambiguous results. We next analyzed the degradation efficacy of **5a** and **5c** in a time-course experiment at the concentration of 10 μM with 3, 6, 18, 24, 30 and 48 h time points (Fig. 2B–C). **5a** showed a peak of degradation at 6 and 18 h. α-tubulin is strongly acetylated at 3, 30 and 48 h (Fig. 2B). **5c** showed a similar profile to that of **5a**, but in this case the best degradation was observed at 18 and especially at 24 h of incubation (Fig. 2C) at 10 μM. **5a** and **5c** were further tested in the same conditions at 1 μM concentration (Fig. 2D and E). As shown in Fig. 5D and a was not able to degrade HDAC6 at this concentration and

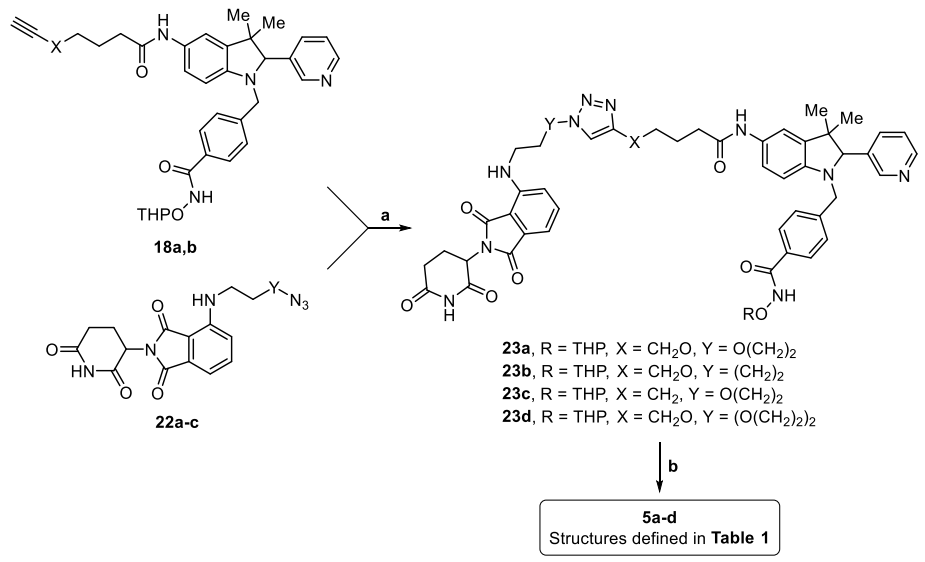

Scheme 4. Reagents and conditions: **a**) $Cu(OAc)_2$, sodium ascorbate, dry DMF, H_2O, rt, 20 h, 25–82 %; **b**) HCOOH 88 %, rt, 10 min, 11–30 %.

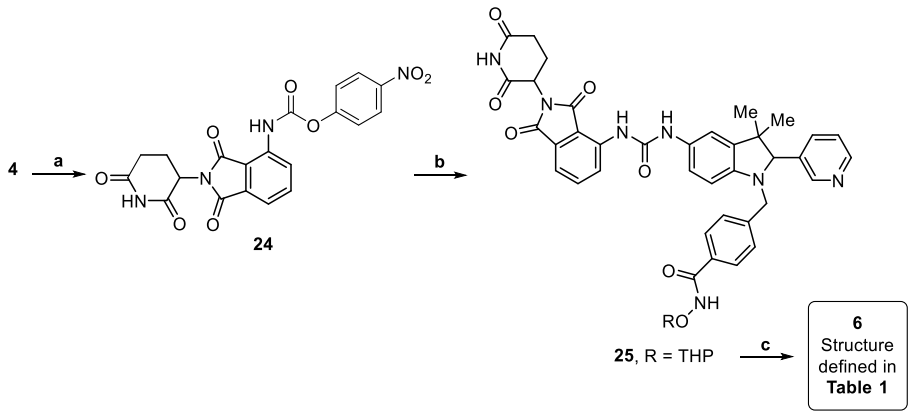

Scheme 5. Reagents and conditions: **a**) 4-nitrophenyl chloroformate, dry THF, 80 °C, 14 h; **b**) **14**, TEA, dry THF, 60 °C, 4 h, 68 % over two steps; **c**) 88 % HCOOH, rt, 10 min, 20 %.

displayed a marked acetylation of α-tubulin only after 48 h of incubation. Analogously, **5c** did not seem to significantly promote degradation of HDAC6 at this concentration (Fig. 2E). Overall, time-course experiments at 10 μM data prompted us to further investigate the arrangement of the ternary complexes produced by **5a** by means of molecular modelling studies using the "linkerless" compound **6** as negative control.

2.4. Prediction of ternary complexes by molecular modelling investigations

To identify a possible arrangement of the ternary complex involving HDAC6, CRBN and newly synthesized PROTACs, molecular modelling investigations (Fig. 3) were performed starting from the X-ray structures of *h*HDAC6 bound to trichostatin A [45] and CRBN [46] in complex with lenalidomide, representing the CRBN-binding scaffold of the PROTACs herein synthesized.

The investigation began by generating the complex between *h*HDAC6 and compound **1**, which serves as the HDAC-binding scaffold of the developed PROTACs. Compound **1** had been co-crystallized within the binding site of *zf*HDAC6 [18], providing a structural basis to identify a plausible orientation for the PROTACs exit vector. Docking studies showed that in *h*HDAC6 **1** adopted a binding pose in that was superimposable to the X-ray structure of the *zf*HDAC6–**1** complex. In this binding mode, the oxygen atoms of the hydroxamic acid group, modelled in its neutral form, were engaged in coordination bonds with the Zn^{2+}, and formed hydrogen bonds with His610 and Tyr782 (Fig. S2). In our study, we assumed that the ternary complex might be either generated by the recognition of the PROTAC by HDAC6, followed by the recruitment of CRBN, or by the direct binding of the PROTAC compound to a pre-organized HDAC6-CRBN binary complex. Following the first hypothesis and starting from the docking model of *h*HDAC6 bound to **1**, the title PROTAC **5a** was built by modifying the cap group of the inhibitor. The resulting complex was used to explore the conformational space of **5a** bound to *h*HDAC6 by performing a metadynamics simulation, in which collective variables describing the extension of the linker connecting the HDAC- and the CRBN-binding scaffolds enabled the identification of several conformations of the title PROTAC (see Methods for details). A cluster analysis identified 38 unique arrangements of the linker of **5a** bound to *h*HDAC6, but only in three of them (namely clusters 1, 6 and 9) the CRBN-binding fragment was projected into the solvent, with no *h*HDAC6 residues closer than 8 Å to it. These three *h*HDAC6-**5a** complexes were then used to generate ternary complexes by superposing the lenalidomide-CRBN X-ray structure on the CRBN-binding fragment (pomalidomide-like) present in the title PROTAC bound to *h*HDAC6. This procedure enabled the generation of complexes free of steric clashes between the two proteins, which were then subjected to 400 ns-long molecular dynamics (MD) simulations. Analysis of the trajectories showed that, in all the three models, the two

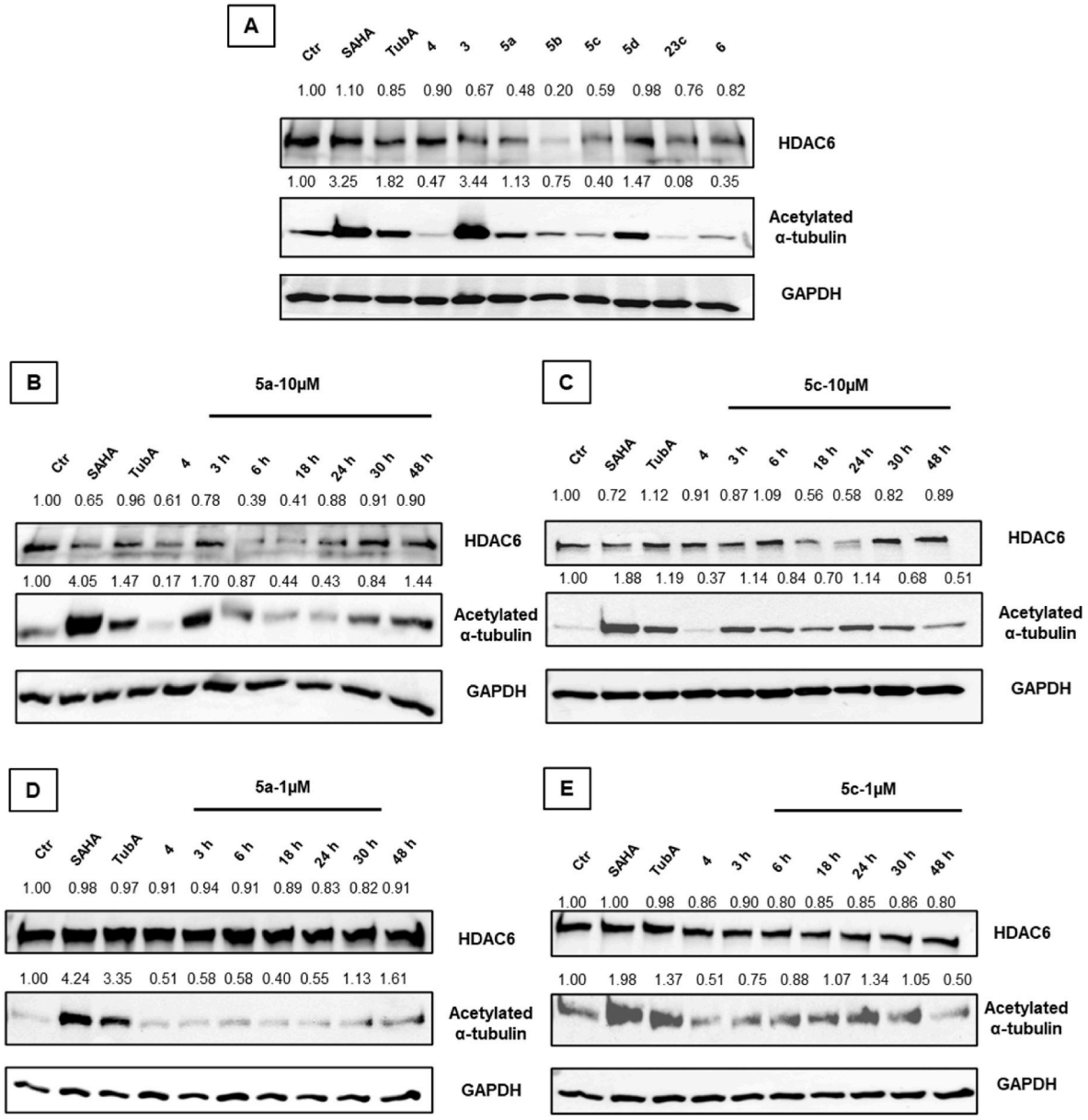

Fig. 2. **A**) Western blot analysis was conducted to assess the expression of HDAC6 and acetylated tubulin in total protein extracts. **B,C**) HDAC6 and acetylated-tubulin detected by Western blot analysis at different time points after **5a** and **5c** at 10 μM concentration. **D,E**) HDAC6 and acetylated-tubulin detected by Western blot analysis at different time points after **5a** and **5c** treatment at 1 μM concentration. Semi-quantitative analysis of the Western blot results was performed using ImageJ software (version 1.44).

HDAC- and CRBN-binding scaffolds maintained stable interactions with HDAC6 and CRBN, while conformational rearrangements of the linker allowed the approaching of the two proteins, leading to the identification of alternative protein-protein interaction modes at the interface between *h*HDAC6 and CRBN. One of the three MD runs (corresponding to cluster 1) showed that after the first 200 ns of simulation the ternary complex could assume a stable conformation (Fig. S3), also featuring the lowest interaction energies calculated for the protein-protein complexes (Fig. S3). To identify relevant protein-protein interactions, a more extensive analysis on the trajectories was performed (Fig. S4). This revealed that the observed conformation was favored by polar contacts between Ser564, Asp567, Gly683, Asp684 and Glu685 of *h*HDAC6 and Leu370, Lys401, Thr405, Lys406 and Lys407 of CRBN, as well as by hydrogen bonds between the PROTAC linker and Arg373 of CRBN and His550 of *h*HDAC6 (Fig. 3A and Figure S5). This computational approach, based on PROTAC conformational analysis and protein superposition, was also applied to investigate the feasibility of the formation of a *h*HDAC6:**6**:CRBN ternary complex. However, the resulting ternary complexes involving compound **6** in two alternative conformations exhibited several backbone–backbone clashes, indicating an interaction between *h*HDAC6 and CRBN that is incompatible with productive ternary complex formation (Fig. 3B and S6). We next evaluated ternary complexes built on the assumption of a preliminary recognition of the ligase (CRBN) and the target protein (*h*HDAC6). To this aim, we integrated the results of the conformational analysis of the PROTAC linker—obtained through metadynamics simulations as described above—with the outcome of a protein–protein docking procedure [47, 48], in which the structure of CRBN was sampled across the surface of *h*HDAC6. This protocol allowed to obtain several ternary complexes for **5a** and **6**, that were ranked considering both the docking score and the disposition of the thalidomide portion of the PROTAC in the binding site of CRBN. More specifically, the first 1000 protein-protein docking poses

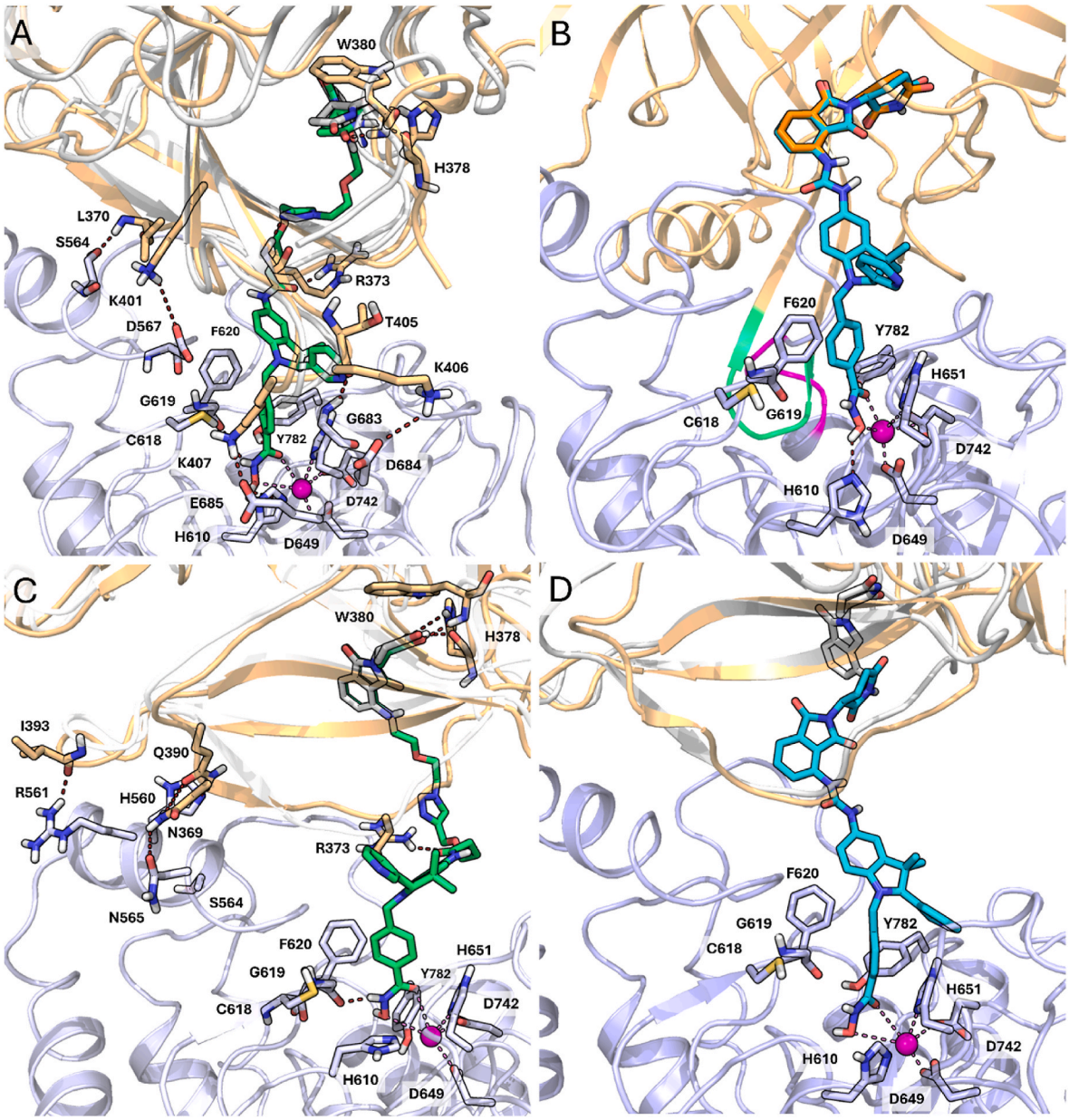

Fig. 3. Molecular models of ternary complexes of HDAC6:**5a**/**6**:CRBN (light blue carbon atoms and cartoon, green/cyan carbon atoms, and orange carbon atoms and cartoon, respectively); chelation bonds and H-bonds are represented with pink and red dashed lines, respectively. **A**) Ternary complex HDAC6:**5a**:CRBN obtained by structure superposition, taken from the MD simulation (cluster 1; geometry extracted at 400 ns of MD simulation); the crystallographic coordinates of CRBN-lenalidomide (grey cartoon and carbon atoms, respectively) are superimposed on the snapshot. **B**) Geometry of the ternary complex HDAC6:**6**:CRBN obtained by structure superposition. Backbone-backbone overlapping regions of the two proteins, involving residues Val503-Arg506 of *h*HDAC6 and Gln148-Glu153 of CRBN, are highlighted in magenta and green, respectively. **C**) Geometry of the ternary complex HDAC6:**5a**:CRBN obtained through the protein-protein docking protocol, taken from the MD simulation (geometry extracted at 400 ns of MD simulation). The crystallographic coordinates of CRBN-lenalidomide (grey cartoon and carbon atoms) are superimposed on the snapshot. **D**). Geometry of the ternary complex HDAC6:**6**:CRBN obtained through the protein-protein docking protocol, taken from the MD simulation (geometry extracted at 400 ns of MD simulation). The crystallographic coordinates of CRBN-lenalidomide (grey cartoon and carbon atoms, respectively) are superimposed on the snapshot.

for docking score were re-ranked according to the root-mean square deviation (RMSD) between the heavy atoms of lenalidomide co-crystallized within CRBN and the corresponding atoms of the thalidomide scaffold in the conformations identified through the meta-dynamics simulation, after superposition on the *h*HDAC6 structure employed for the protein-protein docking. The best ternary complex for each PROTAC was further evaluated through MD simulations. Analysis of the trajectories showed that the *h*HDAC6:**5a**:CRBN complex remained stable throughout the entire MD simulation, with the HDAC- and CRBN-binding portions of the PROTAC maintaining persistent interactions with their respective targets. After the first 150 ns of MD simulation, a rearrangement of the linker of **5a** allowed to retrieve an alternative protein-protein disposition (Fig. S7–S8), mainly stabilized by polar contacts between His560, Arg561, Ser564 and Asn565 of *h*HDAC6 and Asn369, Gln390 and Ile393 of CRBN, as well as by hydrogen bonds between the linker of the PROTAC and Arg373 of CRBN (Fig. 3C and Figure S9). Using this computational approach, analysis of the MD simulation of the HDAC6:**6**:CRBN complex showed that although the two proteins remained associated, the thalidomide moiety of compound **6** failed to maintain its initial binding pose and drifted out of the CRBN

binding cavity (Fig. 3D). Both computational strategies allowed us to identify possible ternary complexes that account for the significant ability of **5a** to induce HDAC6 degradation in cells and the lack of activity displayed by **6** in the same experimental conditions. It is also worth noting that MD simulations performed on HDAC6:**5a**:CRBN ternary complexes obtained with two alternative computational approaches provided comparable results. The analysis of the interface between *h*HDAC6 and CRBN in representative equilibrated snapshots (i.e., structures extracted at 400 ns of MD simulation) outlined that the area of the protein-protein interface was superimposable in the two models, and comprised common regions in both *h*HDAC6 (residues of the helix delimited by residues Thr556 and Asn565, in close contact with L1 loop of the enzyme) and CRBN (residues of the β-sheet core of CRBN thalidomide-binding domain; Figure S10).

2.5. Antifibrotic effects of 5a and 5c in in vitro model of pulmonary fibrosis

2.5.1. The new degraders modulate HDAC6 machinery in IMR-90 human lung fibroblasts

Isoform HDAC6 was selected as the prevalent isoform involved in fibrotic transition of lung cells as demonstrated by us and others [16–19]. To study the ability of PROTACs **5a** and **5c** to degrade HDAC6 in IMR-90 fibroblasts, Western blot analysis of the target protein was performed (Fig. 4). The degradation activity of HDAC6 PROTACs **5a** and **5c** was tested at 18 and 24 h. Molecular analysis demonstrated that HDAC6 levels remained stable up to 18 h of treatment. However, at 24 h, a significant reduction was observed, particularly in cells exposed to 1 μM of **5a** (Fig. 4A). Compound **5c** exhibited lower activity in HDAC6 degradation (Fig. 4A and B vs **4C** and **4D**), while the concentration of 0.1 μM was ineffective for both PROTACs (Fig. 4A–D). To further validate the target of the PROTACs under investigation, the downstream signaling of HDAC6 was examined. Western blot analysis was conducted to assess the downstream effects of HDAC6 degradation, specifically

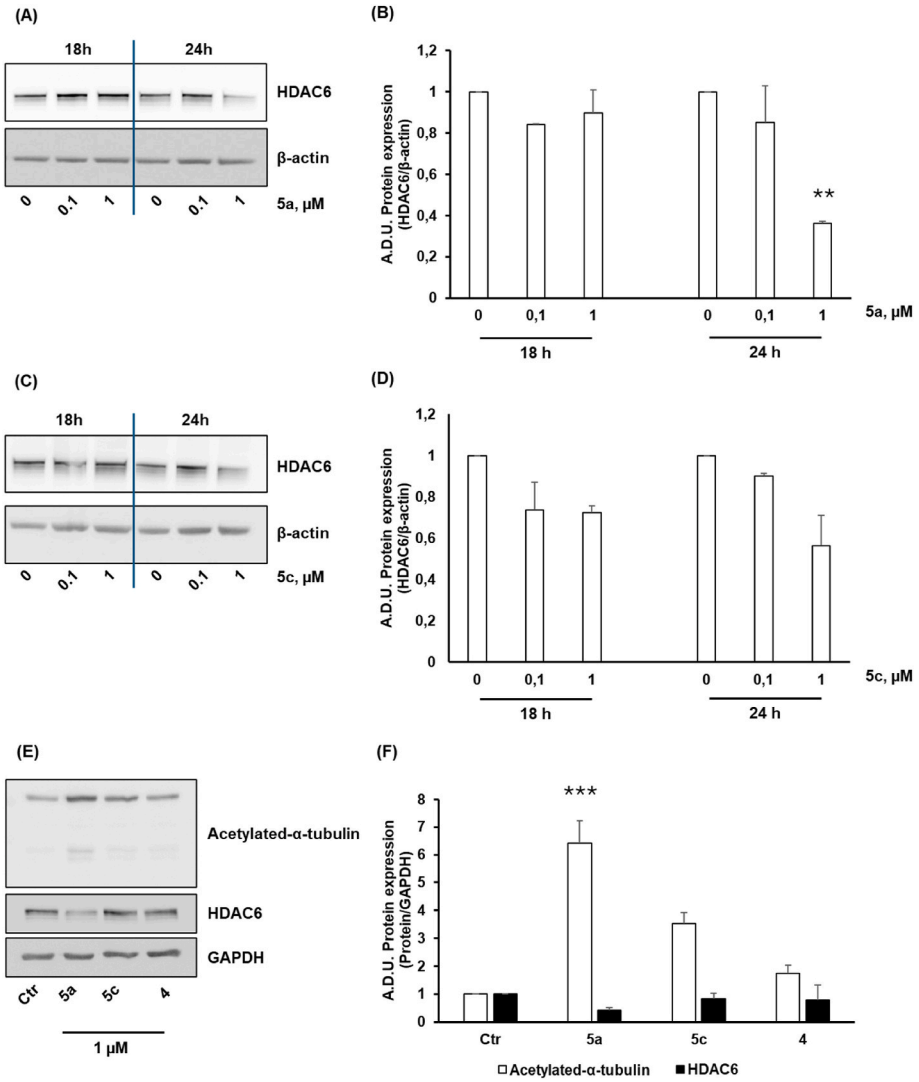

Fig. 4. PROTACs degrade HDAC6 in vitro. Degradation of HDAC6 was evaluated in IMR-90 cells exposed to two PROTACs **5a** and **5c** at different concentrations (0.1 and 1 μM) at 18 and 24 h. **A**) HDAC6 expression in IMR-90 treated with **5a** (0.1 and 1 μM) for 18 and 24 h. **B**) Quantification of blot in (A). Densitometry Units (A.D.U.) ± SD were reported as HDAC6 vs β-actin (n = 2). *p < 0.05 and **p < 0.01 vs untreated cells (Ctr). **C**) HDAC6 levels in IMR-90 treated with **5c** (0.1 and 1 μM) for 18 h and 24 h. **D**) Quantification of blot in (B). Densitometry Units (A.D.U.) ± SD were reported as HDAC6 vs β-actin (n = 2). **E**) Protein analysis of acetylated α-tubulin and HDAC6 in IMR-90 treated with PROTACs or **4** at 1 μM. **F**) Quantification of blot in (E). Densitometry Units (A.D.U.) ± SD were reported as Protein vs GAPDH (n = 2). ***p < 0.001 vs untreated cells (Ctr).

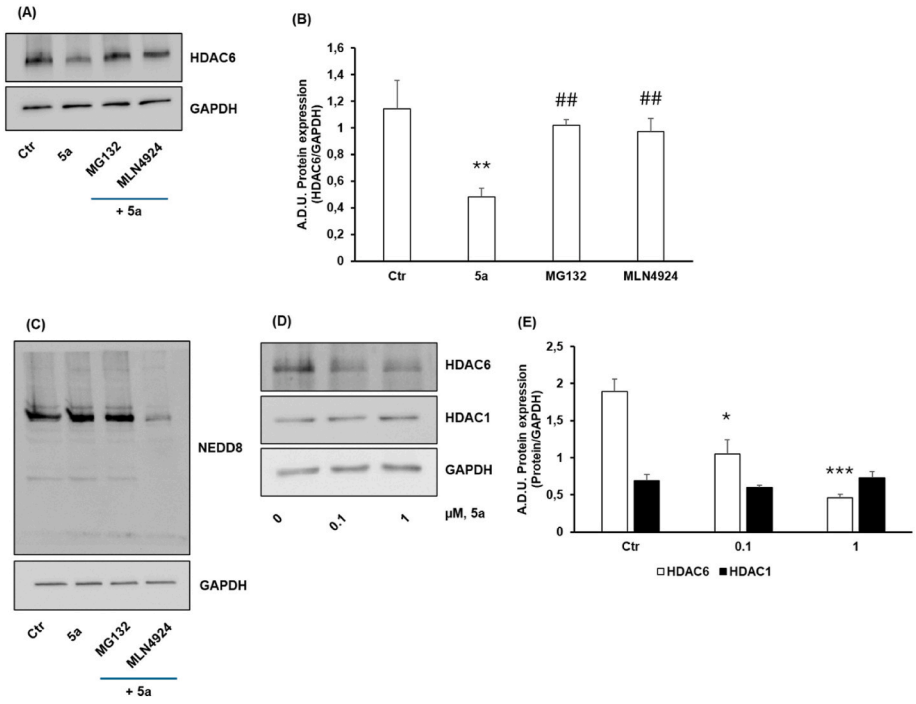

Fig. 5. Mechanism of action of HDAC6 degradation by 5a. A) Representative Western blot showing HDAC6 protein levels in IMR-90 cells pre-treated with MG132 (0.1 μM) or MLN4924 (0.1 μM) for 30 min, followed by exposure to **5a** (1 μM) for 24 h. **B**) Quantification of blot in A. Densitometry Units (A.D.U.) ± SD were reported as HDAC6 vs GAPDH. (n = 3). **p < 0.01 vs untreated cells (Ctr). ##p < 0.01 vs **5a**. **C**) Western blot analysis of NEDD8-conjugated proteins. GAPDH was used as loading control. **D**) Western blot analysis of HDAC6 and HDAC1 in IMR-90 cells treated with increasing concentrations of **5a** (0.1 μM and 1 μM) for 24 h in medium containing 2 % FBS. **E**) Quantification of blot in D. Densitometry Units (A.D.U.) ± SD were reported as HDAC6 and HDAC1 vs GAPDH. (n = 3). *p < 0.05 and ***p < 0.001 vs. untreated cells (Ctr).

evaluating α-tubulin acetylation. The results showed that **5a**, which significantly degrades the deacetylase expression, caused a statistically significant increase in acetylated α-tubulin (Fig. 4E–F). Again, the effects of PROTAC **5c** were less pronounced. Additionally, pomalidomide was unable to induce degradation of the HDAC6 protein in IMR-90, though a slight increase in α-tubulin acetylation was observed. (Fig. 4E–F).

2.5.2. 5a recruits HDAC6, but not HDAC1, for degradation via the CRBN–CRL4–proteasome pathway

Given the higher activity of compound **5a** in promoting HDAC6 degradation, we subsequently focused on investigating the underlying mechanism. Specifically, we examined whether this process is dependent on both proteasomal activity and neddylation. The CUL4-DDB1-RBX1 E3 ubiquitin ligase E3 ligase complex ($CRL4^{CRBN}$), requires neddylation of its cullin subunit (i.e., CUL4) to undergo a conformational change that enables substrate ubiquitination and subsequent proteasomal degradation [49].

Using a pharmacological approach, we dissected the mechanism of HDAC6 degradation triggered by **5a**. MLN4924, an inhibitor of neddylation, was employed to block the activation of $CRL4^{CRBN}$ and impair substrate degradation. In parallel, treatment with the proteasome inhibitor MG132 was used to confirm whether HDAC6 turnover depends on the ubiquitin–proteasome system, as PROTAC-induced degradation ultimately relies on proteasomal clearance of ubiquitinated proteins.

To this aim, IMR-90 cells were pre-treated with the proteasome inhibitor MG132 or the neddylation inhibitor MLN4924 (0.1 μM, 30 min), and subsequently exposed to **5a** for 24 h. HDAC6 protein levels were analyzed by Western blot. MG132 pre-treatment resulted in a marked accumulation of HDAC6, indicating that its degradation occurs via the ubiquitin–proteasome system. Notably, MLN4924 treatment also led to a clear rescue of HDAC6 levels, suggesting that CUL4 recruitment is required for efficient ubiquitination and subsequent proteasomal degradation of HDAC6 (Fig. 5A and B). Western blot analysis for NEDD8 showed a strong reduction in NEDD8 conjugates in cells treated with MLN4924 (0.1 μM), as evidenced by the absence of the typical high molecular weight bands corresponding to NEDD8-modified proteins. In contrast, untreated cells and MG132-treated cells displayed normal NEDD8 conjugation, confirming that MLN4924 effectively inhibits NEDD8 activation and thus neddylation (Fig. 5C). To evaluate the ability of **5a** to degrade other HDAC isoforms, we focused on the analysis of HDAC1, as it emerged as the primary potential off-target based on results from enzymatic assays conducted on isolated enzymes (see Table 1). As shown in Fig. 5D and E, **5a** induces maximal degradation of HDAC6 at 1 μM after 24 h of treatment, whereas no reduction in HDAC1 expression was observed.

Altogether, these results suggest that **5a** selectively targets HDAC6, but not HDAC1, for proteasomal degradation in a CRL-dependent manner. Experiments were conducted to assess the selectivity of PROTAC **5a**, particularly by evaluating the degradation of HDAC6 in comparison to HDAC1, and no significant changes in HDAC1 expression were observed [40].

2.5.3. HDAC6 PROTACs reduce TGF-β1-induced fibrosis via a proteasome-dependent mechanism

To evaluate the role of HDAC6 in the pulmonary fibrosis process, an *in vitro* fibrosis model was developed using IMR-90 fibroblasts (Fig. 6). Exposure of IMR-90 fibroblasts to TGF-β1 induced drastic phenotypic changes, with the exposed cells adopting a flattened morphology respect to the more lengthened/elongated untreated cells (Fig. 6A). However, the co-treatment with HDAC6 PROTACs showed minimal effect on cell morphology. Interestingly, molecular analysis revealed a strong induction of fibronectin by TGF-β1, which was significantly reduced by co-treatment with **5a** and **5c** (Fig. 6B and C). The pattern of fibronectin reduction aligns with HDAC6 degradation, as the decrease in deacetylase levels is more pronounced in fibroblasts treated with **5a (**Fig. 6B and C**)**. Although α-SMA is induced by TGF-β1, we failed to observe a

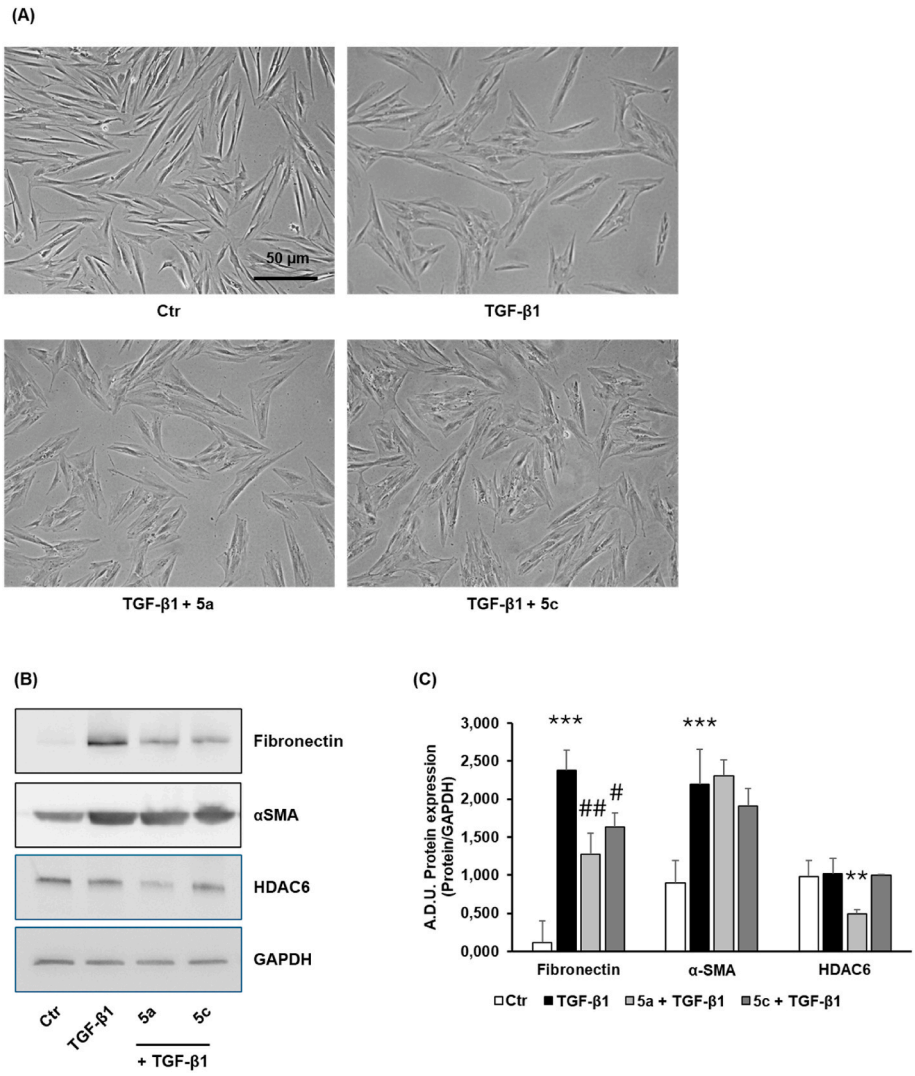

Fig. 6. 5a and 5c attenuate TGF-β1-induced lung fibrosis in vitro. A) Morphology of IMR-90 exposed to TGFβ-1 (5 ng/mL) and PROTACs (**5a** and **5c**, 1 μM) for 48 h. Scale bar, 50 μm. **B**) Western blot analysis of fibrosis markers in IMR-90 exposed to TGF-β1 (5 ng/mL) and PROTACs **5a** and **5c** for 48 h. **C**) Quantification of blot in (B). Densitometry Units (A.D.U.) ± SD were reported as Protein vs GAPDH (n = 2). **p < 0.01 and ***p < 0.001 vs untreated cells (Ctr). #p < 0.05 and ##p < 0.01 vs TGF-β1 alone.

reduction in its levels in the presence of HDAC6 PROTACs (Fig. 6B and C). Therefore, an analysis of the intracellular organization of the protein was conducted, as the formation of stress fibers is a characteristic feature of fibrosis. Immunofluorescence analysis reported in Fig. 7A demonstrated that TGF-β1 incorporated α-SMA into stress fibers, enhancing the contractile activity of myofibroblasts. Co-treatment with **5a**, and to a lesser extent **5c**, disrupted the fibers, rendering them less organized. To demonstrate that HDAC6 degradation caused by **5a** was dependent on the ubiquitin-proteasome system, we repeated the fibrosis experiments in the presence of the proteasome inhibitor MG-132. As shown in Fig. 7B and C, co-treatment with MG-132 reduced and reversed the inhibition of HDAC6 and restored the expression of fibronectin induced by TGF-β1.

3. Conclusions

This study represents the first application of PROTAC technology in a cell-based model mimicking IPF, paving the way for the development of therapeutic degraders aimed at reverting the fibrotic transition. We demonstrated that not only HDAC6 inhibition but also its proteasome-mediated degradation, under exposure of **5a** and **5c**, may represent an innovative strategy to revert the fibrotic phenotype.

The data herein reported confirm that compounds **5a** and **5c** promote HDAC6 degradation in both A549 lung cancer cells and IMR-90 human lung fibroblasts. Two different computational approaches were exploited to model and predict the formation of ternary complexes between HDAC6, PROTAC tools, and E3 ligase. Functionally, compounds **5a** and **5c** reversed the fibrotic phenotype induced by TGF-β1 in IMR-90 cells, as evidenced by a reduction in the pro-fibrotic marker fibronectin expression and disruption of highly organized α-SMA fibers, effects that paralleled the decrease in HDAC6 protein levels. **5a** was not able to degrade HDAC6 in the presence of the proteasome inhibitor MG-132 or neddylation inhibitor MLN4924, thus validating the proteasome- and CRBN-mediated mechanism of action associated with these new PROTACs. Notably, HDAC1 levels remained unaffected, suggesting a degree selectivity for these HDAC6-targeting PROTACs. These findings not only support the mechanism of action of **5a** and **5c** as HDAC6 degraders but also highlight their therapeutic potential as anti-fibrotic agents. Further studies in ex vivo and in vivo models of idiopathic pulmonary fibrosis (IPF) will be crucial to fully validate their efficacy and translational relevance.

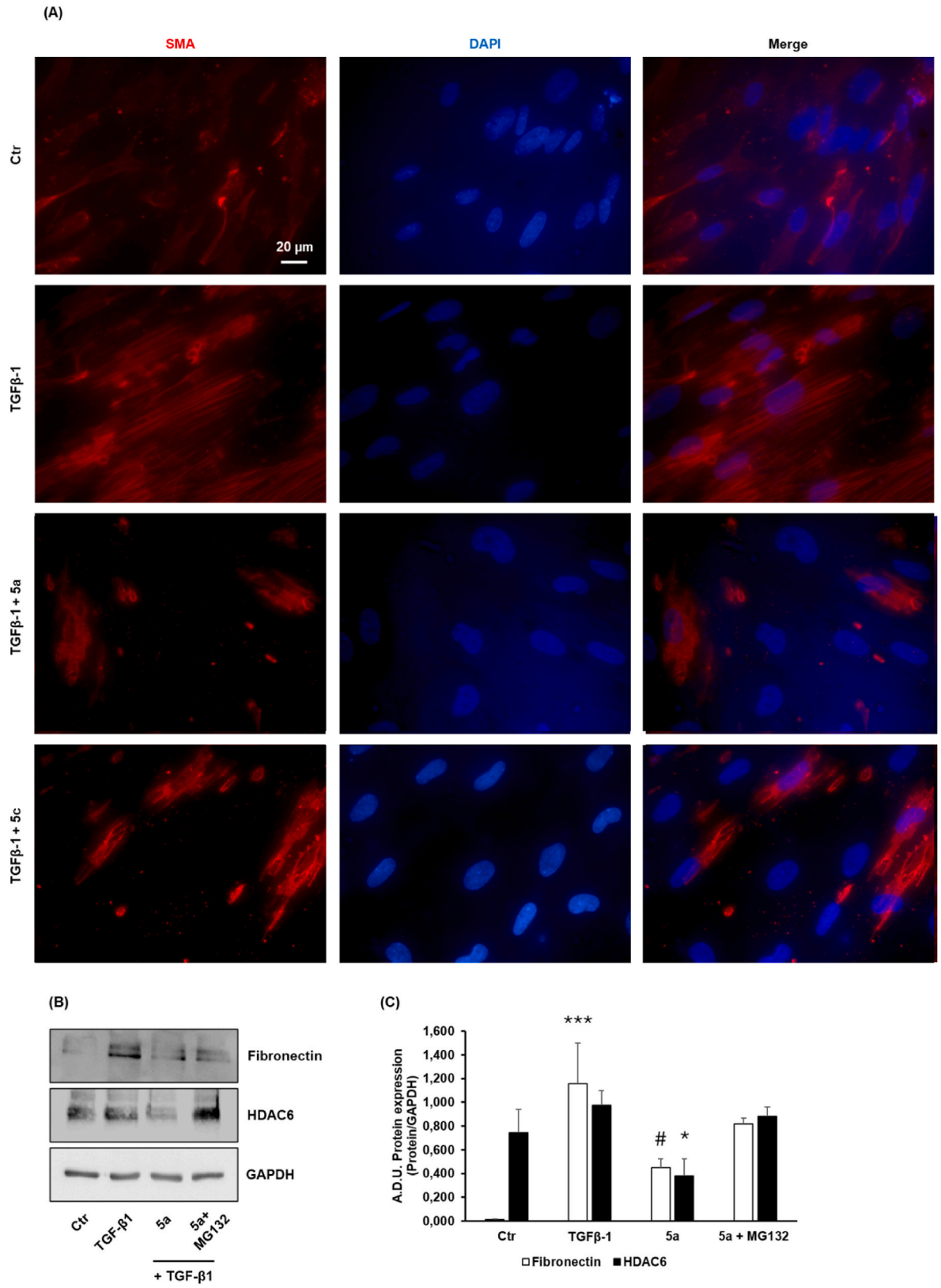

Fig. 7. Immunofluorescence and validation of the PROTAC-mediated antifibrotic effect. (A). Immunofluorescence analysis for α-SMA in IMR-90 exposed to TGFβ-1 (5 ng/mL) and PROTACs **5a** and **5c** for 48 h. Scale bar: 20 μm. (**B,C**). Western blot analysis of fibronectin and HDAC6 in IMR-90 exposed to TGF-β1 (5 ng/mL) and PROTACs **5a** with or without MG-132 (pre-treatment of 30 min) for 48 h (n = 2). *$p < 0.05$ and ***$p < 0.001$ vs untreated cells (Ctr). #$p < 0.05$ vs TGF-β1 alone.

4. Materials and methods

4.1. Chemistry

Reaction progress was monitored by TLC using silica gel 60 F254 (0.040−0.063 mm) with detection by UV (254 nm). All reagents were purchased from commercial suppliers and used without further purification. All moisture-sensitive reactions were performed under a nitrogen atmosphere using oven-dried glassware and dry solvents. Dry tetrahydrofuran (THF) was freshly distilled from sodium/benzophenone, while dichloromethane (DCM) and *N*,*N*-dimethylformamide (DMF) were freshly distilled from calcium hydride and stored under argon atmosphere.

Flash column chromatography was carried out on silica gel (Merck: Kieselgel 60, particle size 0.040–0.063 mm). Reactions' progression was monitored by thin-layer chromatography (TLC), carried out using glass-backed plates coated with Merck Kieselgel 60 GF254. Plates were visualized under UV light (at 254 and 366 nm) or by staining with potassium permanganate, ninhydrin, or cerium ammonium molybdate followed by heating. ^{1}H NMR and ^{13}C NMR spectra were recorded on a Varian 300 MHz spectrometer using the residual signal of the deuterated solvent as an internal standard. Coupling constants (*J*) are given in hertz (Hz). Splitting patterns are described as singlet (s), doublet (d), triplet (t), quartet (q), multiplet (m), and broad (br); the value of chemical shifts (δ) is given in parts per million (ppm) [50]. Mass spectra were recorded utilizing an electron spray ionization (ESI) Agilent 1100 Series LC/MSD spectrometer. ESI-HRMS spectra were acquired by a linear iontrap-Orbitrap hybrid mass spectrometer (LTQ Orbitrap XL) (Thermo Fisher Scientific) operating in positive electrospray ionization mode. Data was collected and analyzed using the Xcalibur 2.2 software provided by the manufacturer [51,52]. Yields refer to purified products and are not optimized. Target compounds were analyzed by LC-MS analysis on an Agilent 1260 Infinity II LC/MSD iQ instrument to confirm purity >95 %. The chromatographic separation was carried out using a gradient of (A) 0.1 % formic acid in water and (B) 0.1 % formic acid in acetonitrile. The gradient conditions were as follows: 0–10 min, 5–95 % B; 10–14 min, 95 % B, 14–15 min, return to 5 % B, 15–18 min, 5 % B. The flow rate was 0.20 mL/min, and the column temperature was set at 30 °C. Mass spectrometry detection was conducted using an ESI source in positive ion mode. Full-scan data were acquired over the *m/z* range of 100–1000.

4.1.1. General procedure A: copper-catalyzed azide-alkyne cycloaddition (CuAAC)

To a stirring solution of the suitable alkyne (0.11 mmol) and azide (0.1 mmol) intermediates in dry DMF (1 mL) under a N_2 atmosphere, a freshly prepared mixture of $Cu(OAc)_2$ (0.027 mmol) and sodium ascorbate (0.064 mmol) in water under a N_2 atmosphere was added dropwise. The reaction mixture was stirred at rt for 16 h. Then, the solvent was removed by co-evaporation with n-heptane under reduced pressure.

4.1.2. General procedure B: O-THP deprotection

The *O*-THP-protected hydroxamic acid (0.1 mmol) was treated with an 88 % solution of formic acid (1 mL), and the solution was stirred at rt for 10–30 min. Then, water was added, and the precipitate was collected by filtration.

4.1.3. 2-Methyl-1-(pyridin-3-yl)propan-1-one (**8**)

Tosylhydrazone **7** (610 mg, 2.70 mmol) and Cs_2CO_3 (1317 mg, 4.04 mmol) were dissolved in 1,4-dioxane (10 mL) in a reaction tube. The tube was backfilled with nitrogen. Then, 3-pyridincarboxaldehyde (253 μL, 2.70 mmol) was added. The tube was sealed and heated to 110 °C for 18 h. The reaction was cooled to rt, quenched with a saturated solution of NH_4Cl (30 mL), and extracted with DCM (3 × 20 mL). The combined organic layers were dried over anhydrous Na_2SO_4, and the solvents were removed under reduced pressure to give a residue that was purified by flash column chromatography on silica gel (3:1 petroleum ether/EtOAc), affording the title compound as a colorless oil (60 % yield). ESI-MS *m/z*: 150 $[M+H]^+$.^{1}H NMR (300 MHz, $CDCl_3$) δ 9.11 (s, 1H), 8.72 (d, J = 4.8 Hz, 1H), 8.23−8.13 (m, 1H), 7.44−7.33 (m,1H), 3.60−3.36 (m, 1H), 1.20 (s, 3H), 1.18 (s, 3H).

4.1.4. 3,3-Dimethyl-5-nitro-2-(pyridin-3-yl)-3H-indole (**9**)

To a solution of **8** (50 mg, 0.34 mmol) in 12 N HCl (750 μL), 4-nitrophenylhydrazine (51 mg, 0.34 mmol) was added. The reaction mixture was heated at 70 °C for 18 h. After completion, the reaction mixture was allowed to reach rt, and the solids were removed by filtration, washing with H_2O. The filtrate was treated with a saturated solution of $NaHCO_3$ until pH = 9, obtaining an opalescent suspension, which was extracted with EtOAc (3 x 10 mL). The combined organic layers were dried over anhydrous Na_2SO_4, filtered and evaporated under reduced pressure to give a residue, which was purified by column chromatography on silica gel (3:1 to 2:1 petroleum ether/EtOAc), obtaining the title compound as a yellow solid (45 % yield). ESI-MS *m/z*: 268 $[M+H]^+$, 290 $[M+Na]^+$. ^{1}H NMR (300 MHz, $CDCl_3$) δ 9.35 (s, 1H), 8.80–8.72 (m, 1H), 8.51 (dd, J = 8.2, 1.9 Hz, 1H), 8.31 (dt, J = 8.5, 1.8 Hz, 1H), 8.26–8.20 (m, 1H), 7.77 (dd, J = 8.6, 1.4 Hz, 1H), 7.47 (dd, J = 8.2, 4.8 Hz, 1H), 1.66 (d, J = 1.4 Hz, 6H).

4.1.5. 3,3-Dimethyl-5-nitro-2-(pyridin-3-yl)indoline (**10**)

A 1.0 M solution of catecholborane in THF (5.28 mL) was added to compound **9** (373 mg) at rt. Then, the reaction mixture was cooled to 0 °C, and TFA was added dropwise (1.32 mL). After stirring for 5 min at 0 °C, the reaction was monitored by ESI-MS, indicating complete conversion, followed by quenching with 1N NaOH (10 mL) and extraction with EtOAc (3 x 10 mL). The combined organic layers were backwashed with 1N NaOH (3 x 30 mL), dried over anhydrous Na_2SO_4, filtered and evaporated under reduced pressure (yellow solid, 99 % yield). ESI-MS *m/z*: 270 $[M+H]^+$, 292 $[M+Na]^+$. ^{1}H NMR (300 MHz, $CDCl_3$) δ 8.62–8.52 (m, 2H), 8.04 (dd, J = 8.7, 2.3 Hz, 1H), 7.89 (d, J = 2.3 Hz, 1H), 7.72 (dt, J = 8.0, 2.0 Hz, 1H), 7.31 (dd, J = 7.9, 4.8 Hz, 1H), 6.65 (d, J = 8.7 Hz, 1H), 5.09 (br, 1H), 4.76 (d, J = 1.9 Hz, 1H), 1.47 (s, 3H), 0.77 (s, 3H).

4.1.6. 4-(Bromomethyl)-N-((tetrahydro-2H-pyran-2-yl)oxy)benzamide (**12**)

A solution of **11** (100 mg, 0.47 mmol), *O*-(tetrahydro-2*H*-pyran-2-yl) hydroxylamine (55 mg, 0.47 mmol), and EDC-HCl (107 mg, 0.56 mmol) in dry DCM/DMF 7:1 (3.7 mL) was stirred at rt for 16 h, under N_2 atmosphere. Then, the reaction mixture was treated with 15 mL of a saturated solution of NH_4Cl and extracted with EtOAc (3 x 10 mL). The combined organic layers were washed with a saturated solution of NaCl (3 x 10 mL), dried over anhydrous Na_2SO_4, filtered and evaporated under reduced pressure. The crude was purified by column chromatography on silica gel (2:1 to 1:1 petroleum ether/EtOAc) to yield the title compound as an off-white waxy solid (99 % yield). ^{1}H NMR (300 MHz, $CDCl_3$) δ 9.53 (d, J = 13.8 Hz, 1H), 7.73 (d, J = 6.7 Hz, 2H), 7.38 (d, J = 8.2 Hz, 2H), 5.07–5.00 (m, 1H), 4.55 (s, 2H), 3.98 (td, J = 10.3, 8.9, 2.9 Hz, 1H), 3.66–3.52 (m, 1H), 1.79 (t, J = 7.4 Hz, 3H), 1.57 (d, J = 12.5 Hz, 3H).

4.1.7. 4-((3,3-Dimethyl-5-nitro-2-(pyridin-3-yl)indolin-1-yl)methyl)-N-((tetrahydro-2H-pyran-2-yl)oxy)benzamide (**13**)

To a solution of **10** (100 mg, 0.37 mmol) in dry DMF (2 mL), cooled at 0 °C and under a N_2 atmosphere, NaH-60 % dispersion of in mineral oil (30 mg, 0.74 mmol) was added. The reaction mixture was stirred at 0 °C for 1 h. Then, a solution of **12** (117 mg, 0.37 mmol) in dry DMF (2 mL) was added dropwise at 0 °C. Then, the mixture was allowed to reach rt and was stirred for 18 h. Water (15 mL) was added, and the organic products were extracted with EtOAc (3 x 10 mL). The combined organic layers were washed with a saturated solution of NaCl (3 x 30 mL), dried

over anhydrous Na_2SO_4, filtered and evaporated under reduced pressure to give the desired product as a yellow solid (99 % yield). ESI-MS *m/z*: 503 $[M+H]^+$, 525 $[M+Na]^+$, 541 $[M+K]^+$. ^1H NMR (300 MHz, $CDCl_3$) δ 8.91 (s, 1H), 8.62 (s, 1H), 8.44 (s, 1H), 8.11 (dd, J = 8.8, 2.3 Hz, 1H), 7.92 (d, J = 2.3 Hz, 1H), 7.70 (d, J = 7.9 Hz, 2H), 7.52 (s, 1H), 7.34 (d, J = 7.8 Hz, 1H), 7.18 (d, J = 7.8 Hz, 2H), 6.50 (d, J = 8.9 Hz, 1H), 5.08 (s, 1H), 4.61 (d, J = 16.2 Hz, 1H), 4.45 (s, 1H), 4.21–4.05 (m, 1H), 4.00 (t, J = 10.0 Hz, 1H), 3.72–3.59 (m, 1H), 1.94–1.76 (m, 3H), 1.64 (d, J = 14.7 Hz, 3H), 1.44 (s, 3H), 0.87 (s, 3H).

*4.1.8. 4-((5-Amino-3,3-dimethyl-2-(pyridin-3-yl)indolin-1-yl)methyl)-N-((tetrahydro-2H-pyran-2-yl)oxy)benzamide (**14**)*

To a solution of **13** (212 mg, 0.42 mmol) in 7:1 EtOH/H_2O (3.3 mL), Fe powder (94 mg, 1.69 mmol) and NH_4Cl (90 mg, 1.69 mmol) were added. The reaction mixture was refluxed for 3 h, then allowed to reach rt, and filtered through a Celite pad, washing with MeOH. The residue was dried under reduced pressure, treated with H_2O (10 mL), and extracted with EtOAc (3 x 10 mL). The combined organic layers were dried over anhydrous Na_2SO_4, filtered and evaporated under reduced pressure. The crude was purified by column chromatography on silica gel (10:1 DCM/MeOH) to afford the title compound as a beige solid (85 % yield). ESI-MS *m/z*: 473 $[M+H]^+$, 495 $[M+Na]^+$. ^1H NMR (300 MHz, Acetone-d_6) δ 8.65–8.49 (m, 2H), 7.99–7.75 (m, 3H), 7.53–7.33 (m, 3H), 6.84 (s, 1H), 6.73 (d, J = 8.3 Hz, 1H), 6.51 (dd, J = 8.3, 3.9 Hz, 1H), 5.08 (d, J = 3.0 Hz, 1H), 4.46 (d, J = 17.8 Hz, 1H), 4.07 (dd, J = 14.6, 6.2 Hz, 2H), 3.59–3.47 (m, 2H), 1.89–1.69 (m, 3H), 1.59–1.50 (m, 3H), 1.40 (s, 3H), 0.83 (s, 3H).

*4.1.9. 4-((5-Amino-3,3-dimethyl-2-(pyridin-3-yl)indolin-1-yl)methyl)-N-hydroxybenzamide (**3**)*

14 was dissolved in MeOH (1 mL) and treated with 1 N methanolic hydrogen chloride (250 μL) at rt. After 3 h, the solvent was removed. Purification by column chromatography on silica gel (20:1:0 to 10:1:0.1 DCM/MeOH/NH_4OH) afforded the title compound as a yellow solid (67 % yield) ^1H NMR (300 MHz, CD_3OD) δ 8.63–8.40 (m, 2H), 8.01–7.82 (m, 1H), 7.67 (d, J = 8.1 Hz, 2H), 7.48–7.27 (m, 3H), 6.65 (s, 1H), 6.53 (d, J = 8.3 Hz, 1H), 6.30 (d, J = 8.2 Hz, 1H), 4.37–4.17 (m, 2H), 3.98 (d, J = 16.2 Hz, 1H), 1.36 (s, 3H), 0.78 (s, 3H). ^{13}C NMR (75 MHz, CD_3OD) δ 166.6, 148.7, 148.1, 144.1, 142.7, 139.2, 138.4, 137.1, 134.4, 130.8, 127.4, 126.9, 123.7, 115.4, 111.6, 109.5, 78.3, 52.2, 44.4, 25.0, 24.1.

*4.1.10. 4-(Prop-2-yn-1-yloxy)butanoic acid (**16**). To a stirred mixture of ethyl 4-bromobutanoate (**15**, 205 mg, 1.05 mmol), 10 M aqueous NaOH (200 mg, 5 mmol, 500 μL) and TBAI (39 mg, 0.11 mmol), propargyl alcohol (71 mg, 1.26 mmol) was added dropwise*

The reaction mixture was stirred at 50 °C for 18 h, then monitored by TLC and allowed to cool to rt. The mixture was treated with a saturated solution of NaCl (10 mL) and extracted with EtOAc (3 x 10 mL). The combined organic layers were dried over anhydrous Na_2SO_4, filtered and evaporated under reduced pressure to furnish the desired product as a colorless liquid in 74 % yield. ESI-MS *m/z*: 141 $[M-H]^-$. ^1H NMR (300 MHz, Acetone-d_6) δ 10.33 (br, 1H), 4.13 (d, J = 2.4 Hz, 2H), 3.54 (t, J = 6.3 Hz, 2H), 2.90 (t, J = 2.4 Hz, 1H), 2.38 (t, J = 7.4 Hz, 2H), 1.92–1.77 (m, 2H).

*4.1.11. 4-((3,3-Dimethyl-5-(4-(prop-2-yn-1-yloxy)butanamido)-2-(pyridin-3-yl)indolin-1-yl)methyl)-N-((tetrahydro-2H-pyran-2-yl)oxy) benzamide (**18a**)*

To a mixture of **16** (30 mg, 0.21 mmol) and **14** (83 mg, 0.18 mmol) in MeCN (4 mL), EDC-HCl (34 mg, 0.18 mmol), HOBt (2.4 mg, 0.02 mmol), DMAP (22 mg, 0.18 mmol), and DIPEA (153 μL, 0.88 mmol) were sequentially added. The reaction mixture was stirred at rt for 20 h and then, solvent was removed. The crude was treated with 10 mL of a saturated solution of $NaHCO_3$ and extracted with EtOAc (3 x 10 mL). The combined organic layers were dried over anhydrous Na_2SO_4. The volatiles were removed under reduced pressure to obtain the title compound as a colorless liquid (98 % yield). ESI-MS *m/z*: 597 $[M+H]^+$. ^1H NMR (300 MHz, $CDCl_3$) δ 9.25 (s, 1H), 8.55 (s, 2H), 7.67 (d, J = 7.9 Hz, 2H), 7.53 (s, 1H), 7.37 (s, 1H), 7.27 (d, J = 6.6 Hz, 2H), 7.00 (dd, J = 8.3, 2.1 Hz, 1H), 6.32 (d, J = 8.3 Hz, 1H), 5.29 (s, 1H), 5.07 (s, 1H), 4.35–4.12 (m, 3H), 4.07–3.92 (m, 2H), 3.67–3.56 (m, 3H), 2.54–2.38 (m, 3H), 1.99 (q, J = 6.5 Hz, 2H), 1.94–1.72 (m, 3H), 1.74–1.50 (m, 3H), 1.36 (s, 3H), 0.79 (s, 3H).

*4.1.12. 4-((5-(Hept-6-ynamido)-3,3-dimethyl-2-(pyridin-3-yl)indolin-1-yl)methyl)-N-((tetrahydro-2H-pyran-2-yl)oxy)benzamide (**18b**)*

To a stirring solution of 6-heptynoic acid (**17**, 15 mg, 0.12 mmol) in dry DMF (2 mL), DIPEA (41 μL, 0.24 mmol) and HATU (54 mg, 0.14 mmol) were added at rt, under a N_2 atmosphere. After 30 min, a solution of **14** (56 mg, 0.12 mmol) in dry DMF (2 mL) was added and the resulting mixture was stirred at rt for 16 h. On completion, 10 mL of a saturated solution of NH_4Cl were added and the mixture was extracted with EtOAc (3 x 10 mL). The combined organic layers were washed with a saturated solution of NaCl (3 x 30 mL), and dried over anhydrous Na_2SO_4, filtered and evaporated under reduced pressure. The crude was purified by column chromatography on silica gel (EtOAc) afforded the title compound as a colorless liquid (77 % yield). ^1H NMR (300 MHz, $CDCl_3$) δ 8.51 (d, J = 16.5 Hz, 2H), 7.69 (t, J = 13.9 Hz, 3H), 7.51–7.15 (m, 4H), 7.02 (d, J = 8.2 Hz, 1H), 6.39 (d, J = 8.1 Hz, 1H), 5.10 (s, 2H), 4.39–4.17 (m, 2H), 4.15–3.93 (m, 4H), 3.76–3.54 (m, 3H), 2.36 (t, J = 7.4 Hz, 2H), 2.24 (td, J = 7.0, 2.7 Hz, 2H), 2.00–1.79 (m, 3H), 1.65–1.59 (m, 3H), 1.38 (s, 3H), 0.79 (s,3H).

*4.1.13. 4-((2-(2-Azidoethoxy)ethyl)amino)-2-(2,6-dioxopiperidin-3-yl) isoindoline-1,3-dione (**22a**)*

To a solution of 4-fluoro-thalidomide (200 mg, 0.72 mmol) and **19** (121 mg, 0.72 mmol) in dry DMSO (4.3 mL), DIPEA (505 μL, 2.90 mmol) was added. The reaction mixture was heated at 80 °C for 16 h. Then, 15 mL of a saturated solution of NH_4Cl was added and the mixture was extracted with EtOAc (3 x 15 mL). The combined organic layers were dried over anhydrous Na_2SO_4, filtered and evaporated under reduced pressure. The residual DMSO was removed by co-evaporation with *n*-heptane. Purification by column chromatography on silica gel (2:1 to 0:1 petroleum ether/EtOAc) afforded to obtain the title compound as a yellow solid (38 % yield). ESI-MS *m/z*: 385 $[M-H]^-$. ^1H NMR (300 MHz, $CDCl_3$) δ 8.16 (br, 1H), 7.50 (t, J = 7.9 Hz, 1H), 7.11 (d, J = 7.1 Hz, 1H), 6.94 (d, J = 8.5 Hz, 1H), 6.48 (t, J = 5.9 Hz, 1H), 4.92 (dd, J = 11.8, 5.4 Hz, 1H), 3.70 (dt, J = 13.9, 5.2 Hz, 4H), 3.50 (q, J = 5.4 Hz, 2H), 3.41 (t, J = 5.1 Hz, 2H), 2.94–2.65 (m, 3H), 2.20–2.07 (m, 1H).

*4.1.14. 4-((2-(2-(2-Azidoethoxy)ethoxy)ethyl)amino)-2-(2,6-dioxopiperidin-3-yl)isoindoline-1,3-dione (**22b**)*

By following the procedure described for **22a**, 4-fluoro-thalidomide (200 mg, 0.72 mmol) and **20** (126 mg, 0.72 mmol) were reacted to obtain **22b**. Purification by column chromatography on silica gel (2:1 to 0:1 petroleum ether/EtOAc) furnished the title compound as a yellow solid (45 % yield). ^1H NMR (300 MHz, $CDCl_3$) δ 8.26 (s, 1H), 7.49 (dd, J = 8.4, 7.3 Hz, 1H), 7.11 (d, J = 7.1 Hz, 1H), 6.93 (d, J = 8.5 Hz, 1H), 6.50 (s, 1H), 4.92 (dd, J = 12.4, 5.3 Hz, 1H), 3.74 (t, J = 5.4 Hz, 2H), 3.72–3.65 (m, 6H), 3.48 (q, J = 5.0 Hz, 2H), 3.39 (t, J = 5.0 Hz, 2H), 2.92–2.85 (m, 1H),2.84–2.68 (m, 2H), 2.15–2.08 (m, 1H).

*4.1.15. 4-((4-Azidobutyl)amino)-2-(2,6-dioxopiperidin-3-yl)isoindoline-1,3-dione (**22c**)*

By following the procedure described for **22a**, 4-fluoro-thalidomide (100 mg, 0.36 mmol) and **21** (41 mg, 0.36 mmol) were reacted to obtain **22c**. Purification by column chromatography on silica gel (2:1 to 0:1 petroleum ether/EtOAc) afforded the title compound as a yellow solid (34 % yield). ^1H NMR (300 MHz, $CDCl_3$) δ 8.48 (s, 1H), 7.58 (t, J = 8.5 Hz, 1H), 7.12 (d, J = 8.6 Hz, 1H), 7.02 (d, J = 7.0 Hz, 1H), 6.51 (t, J = 6.1 Hz, 1H), 5.05 (dd, J = 12.8, 5.5 Hz, 1H), 3. 34–3. 37 (m, 4H), 2.94–2.82 (m, 1H), 2.62–2.52 (m, 2H), 2.06-1.98 (m, 1H), 1.66-1.57 (m,

4H).

4.1.16. 4-((5-(4-((1-(2-(2-((2-(2,6-Dioxopiperidin-3-yl)-1,3-dioxoisoindolin-4-yl)amino)ethoxy)ethyl)-1H-1,2,3-triazol-4-yl)methoxy)butanamido)-3,3-dimethyl-2-(pyridin-3-yl)indolin-1-yl)methyl)-N-((tetrahydro-2H-pyran-2-yl)oxy)benzamide (23a)

Compound **23a** was obtained from compound **18a** (54 mg, 0.09 mmol) and **22a** (30 mg, 0.08 mmol) by following General Procedure A. Purification by column chromatography on silica gel (30:1 to 10:1 DCM/MeOH) afforded the title compound as a yellow solid (33 % yield). ^{1}H NMR (300 MHz, CD_3OD) δ 8.53 (s, 3H), 8.05 (s, 1H), 7.78–7.63 (m, 4H), 7.47 (d, J = 8.4 Hz, 1H), 7.32 (d, J = 18.0 Hz, 1H), 7.11 (d, J = 7.1 Hz, 1H), 6.95 (s, 1H), 6.87 (d, J = 8.5 Hz, 1H), 6.49 (s, 1H), 6.32 (s, 1H), 5.14–5.08 (m, 1H), 4.70–4.42 (m, 4H), 4.23 (s, 2H), 4.05 (s, 2H), 3.83 (s, 2H), 3.64 (dd, J = 10.5, 5.5 Hz, 4H), 3.41 (d, J = 5.3 Hz, 2H), 2.92–2.72 (m, 2H), 2.41 (s, 2H), 1.99 (q, J = 6.5 Hz, 2H), 1.85 (d, J = 13.7 Hz, 4H), 1.60 (d, J = 11.5 Hz, 4H), 1.37 (s, 3H), 1.27 (d, J = 7.9 Hz, 2H), 0.79 (s, 6H).

4.1.17. 4-((5-(5-(1-(2-(2-((2-(2,6-Dioxopiperidin-3-yl)-1,3-dioxoisoindolin-4-yl)amino)ethoxy)ethyl)-1H-1,2,3-triazol-4-yl)pentanamido)-3,3-dimethyl-2-(pyridin-3-yl)indolin-1-yl)methyl)-N-((tetrahydro-2H-pyran-2-yl)oxy)benzamide (23b)

Compound **23b** was obtained from compounds **18a** (38 mg, 0.07 mmol) and **22b** (23 mg, 0.06 mmol) by following General Procedure A. Purification by column chromatography on silica gel (30:1 to 10:1 DCM/MeOH) afforded the title compound as a yellow solid (46 % yield). ^{1}H NMR (300 MHz, CD_3OD) δ 8.49 (s, 2H), 7.72–7.63 (m, 3H), 7.56–7.26 (m, 5H), 7.16–7.00 (m, 3H), 6.44 (t, J = 8.1 Hz, 1H), 5.04 (d, J = 12.5 Hz, 1H), 4.67–4.27 (m, 4H), 4.04 (d, J = 16.1 Hz, 1H), 3.85 (t, J = 4.8 Hz, 2H), 3.62 (d, J = 5.2 Hz, 2H), 3.56–3.41 (m, 2H), 3.22 (dd, J = 17.4, 8.8 Hz, 2H), 2.87–2.56 (m, 4H), 2.31 (dt, J = 14.4, 7.5 Hz, 2H), 2.24–2.00 (m, 2H), 1.78–1.52 (m, 7H), 1.48–1.22 (m, 6H), 1.02 (t, J = 7.4 Hz, 2H), 0.80 (d, J = 3.1 Hz, 3H).

4.1.18. 4-((5-(4-((1-(4-((2-(2,6-Dioxopiperidin-3-yl)-1,3-dioxoisoindolin-4-yl)amino)butyl)-1H-1,2,3-triazol-4-yl)methoxy)butanamido)-3,3-dimethyl-2-(pyridin-3-yl)indolin-1-yl)methyl)-N-((tetrahydro-2H-pyran-2-yl)oxy)benzamide (23c)

Compound **23c** was obtained from compound **18b** (45 mg, 0.08 mmol) and **22a** (27 mg, 0.07 mmol) by following General Procedure A. Purification by column chromatography on silica gel (30:1 to 10:1 DCM/MeOH) afforded the title compound as a pale yellow amorphous solid (45 % yield). ESI-MS m/z: 989 $[M+Na]^+$. ^{1}H NMR (300 MHz, CD_3OD) δ 8.51 (d, J = 10.9 Hz, 2H), 7.90 (d, J = 1.5 Hz, 1H), 7.71 (d, J = 7.9 Hz, 2H), 7.48–7.25 (m, 6H), 7.13–6.92 (m, 4H), 6.43 (d, J = 8.4 Hz, 1H), 5.08 (dd, J = 12.7, 5.4 Hz, 1H), 4.58 (d, J = 3.9 Hz, 2H), 4.43–4.28 (m, 4H), 4.18–3.98 (m, 2H), 3.82 (t, J = 6.8 Hz, 2H), 3.67–3.50 (m, 4H), 2.92–2.77 (m, 2H), 2.74–2.54 (m, 1H), 2.39 (t, J = 7.1 Hz, 2H), 2.12–2.00 (m, 1H), 1.95–1.80 (m, 6H), 1.65–1.49 (m, 5H), 1.36 (s, 3H), 0.78 (s, 3H). ^{13}C NMR (75 MHz, CD_3OD) δ 172.1, 171.7, 167.9, 166.3, 164.9, 160.6, 148.6, 147.1, 138.3, 135.1, 130.7, 129.9, 127.5, 123.6, 122.7, 121.3, 111.2, 90.5, 80.7, 77.3, 76.0, 64.3, 61.9, 54.5, 49.3, 44.4, 38.8, 36.3, 33.1, 28.1, 25.3, 24.9, 24.2, 21.6. LC-MS Rt: 9.357 min, purity 98.5 %, MS: 967.5. HRMS(ESI) m/z $[M+H]^+$ calcd for $[C_{52}H_{59}N_{10}O_9]^+$ 967.4461, found 967.4431; $[M+Na]^+$ calcd for $[C_{52}H_{58}N_{10}O_9Na]^+$ 989.4280, found 989.4245.

4.1.19. 4-((5-(4-((1-(2-(2-(2-((2-(2,6-Dioxopiperidin-3-yl)-1,3-dioxoisoindolin-4-yl)amino)ethoxy)ethoxy)ethyl)-1H-1,2,3-triazol-4-yl)methoxy)butanamido)-3,3-dimethyl-2-(pyridin-3-yl)indolin-1-yl)methyl)-N-((tetrahydro-2H-pyran-2-yl)oxy)benzamide (23d)

Compound **23d** was obtained from compound **18a** (44 mg, 0.07 mmol) and **22c** (29 mg, 0.07 mmol) by following General Procedure A. The crude product was used in the next step without any further purification. ESI-MS m/z: 1049 $[M+Na]^+$.

4.1.20. 4-((5-(4-((1-(2-(2-((2-(2,6-Dioxopiperidin-3-yl)-1,3-dioxoisoindolin-4-yl)amino)ethoxy)ethyl)-1H-1,2,3-triazol-4-yl)methoxy)butanamido)-3,3-dimethyl-2-(pyridin-3-yl)indolin-1-yl)methyl)-N-hydroxybenzamide (5a)

Compound **5a** was obtained from compound **23a** (20 mg, 0.02 mmol) by following General Procedure B. Purification by column chromatography on silica gel (30:1 to 5:1 DCM/MeOH) afforded the title compound as an amorphous yellow solid (30 % yield). ESI-MS m/z: 921 $[M+Na]^+$, 897 $[M-H]^-$, 933 $[M+Cl]^-$. ^{1}H NMR (300 MHz, CD_3OD) δ 8.49 (d, J = 5.6 Hz, 2H), 7.89 (s, 1H), 7.68 (d, J = 8.0 Hz, 2H), 7.57–7.38 (m, 3H), 7.38–7.26 (m, 3H), 7.14–6.99 (m, 3H), 6.42 (d, J = 8.4 Hz, 1H), 5.05 (dd, J = 12.0, 5.4 Hz, 1H), 4.60–4.47 (m, 4H), 4.43–4.28 (m, 2H), 4.04 (d, J = 16.3 Hz, 1H), 3.86 (q, J = 5.1 Hz, 2H), 3.64 (t, J = 5.1 Hz, 2H), 3.48 (dt, J = 19.7, 5.6 Hz, 4H), 2.87–2.66 (m, 3H), 2.37 (t, J = 7.2 Hz, 2H), 2.09 (d, J = 8.4 Hz, 1H), 1.90 (p, J = 6.7 Hz, 2H), 1.37 (s, 3H), 0.79 (s, 3H). ^{13}C NMR (75 MHz, CD_3OD) δ 173.8, 172.3, 170.2, 169.3, 167.8, 166.4, 147.0, 146.9, 144.4, 142.3, 138.3, 136.0, 132.5, 131.0, 130.8, 127.5, 126.9, 124.4, 120.0, 117.0, 115.5, 110.8, 109.8, 108.4, 69.6, 69.1, 63.1, 51.2, 50.0, 44.5, 41.7, 33.1, 30.9, 25.3, 25.2, 24.2, 22.4. LC-MS Rt: 8.619 min, purity 95.7 %, MS: 899.4. HRMS(ESI) m/z $[M+H]^+$ calcd for $C_{47}H_{51}N_{10}O_9$ 899.3835, found 899.3863.

4.1.21. 4-((5-(5-(1-(2-(2-((2-(2,6-Dioxopiperidin-3-yl)-1,3-dioxoisoindolin-4-yl)amino)ethoxy)ethyl)-1H-1,2,3-triazol-4-yl)pentanamido)-3,3-dimethyl-2-(pyridin-3-yl)indolin-1-yl)methyl)-N-hydroxybenzamide (5b)

Compound **5b** was obtained from compound **23b** (27 mg, 0.03 mmol) by following General procedure B. Purification by column chromatography on silica gel (30:1 to 5:1 DCM/MeOH) afforded the title compound as an amorphous yellow solid (11 % yield). ^{1}H NMR (300 MHz, CD_3OD) δ 8.49 (s, 2H), 7.90–7.62 (m, 3H), 7.55–7.18 (m, 6H), 7.03 (d, J = 7.1 Hz, 3H), 6.49–6.37 (m, 1H), 5.06 (dd, J = 12.0, 5.4 Hz, 1H), 4.54 (s, 2H), 4.38 (d, J = 16.5 Hz, 1H), 4.31 (s, 1H), 4.03 (d, J = 16.6 Hz, 1H), 3.87 (s, 2H), 3.64 (s, 2H), 3.54 (dd, J = 12.2, 6.1 Hz, 1H), 3.44 (s, 2H), 2.69 (q, J = 10.2, 6.2 Hz, 2H), 2.49 (t, J = 6.6 Hz, 1H), 2.32 (s, 2H), 2.18 (t, J = 7.6 Hz, 1H), 1.81–1.46 (m, 5H), 1.36 (s, 3H), 0.78 (s, 3H). ^{13}C NMR (75 MHz, CD_3OD) δ 173.4, 171.5, 167.4, 159.0, 152.2, 149.4, 147.1, 138.3, 137.5, 130.8, 129.8, 126.4, 122.3, 116.9, 113.5, 111.3, 110.0, 86.7, 69.5, 59.0, 55.2, 44.4, 39.0, 35.7, 32.0, 29.4, 26.3, 25.0, 23.9, 22.4. LC-MS Rt: 8.738 min, purity 95.1 %, MS: 883.4. HRMS (ESI) m/z $[M+H]^+$ calcd for $[C_{47}H_{51}N_{10}O_8]^+$ 883.3886, found 883.3857; $[M+Na]^+$ calcd for $[C_{47}H_{50}N_{10}O_8Na]^+$ 905.3705, found 905.3682.

4.1.22. 4-((5-(4-((1-(4-((2-(2,6-Dioxopiperidin-3-yl)-1,3-dioxoisoindolin-4-yl)amino)butyl)-1H-1,2,3-triazol-4-yl)methoxy)butanamido)-3,3-dimethyl-2-(pyridin-3-yl)indolin-1-yl)methyl)-N-hydroxybenzamide (5c)

Compound **5c** was obtained from compound **23c** (30 mg, 0.03 mmol) by following General Procedure B. Purification by column chromatography on silica gel (30:1 to 5:1 DCM/MeOH) afforded the title compound as an amorphous yellow solid (25 % yield). ^{1}H NMR (300 MHz, CD_3OD) δ 8.49 (s, 2H), 7.91 (d, J = 1.5 Hz, 1H), 7.68 (d, J = 7.9 Hz, 2H), 7.48–7.23 (m, 6H), 7.10 (dd, J = 8.4, 2.1 Hz, 1H), 6.99 (dd, J = 12.5, 7.7 Hz, 2H), 6.44 (dd, J = 8.4, 1.2 Hz, 1H), 5.09 (dd, J = 12.7, 5.5 Hz, 1H), 4.58 (s, 2H), 4.43–4.29 (m, 4H), 4.03 (d, J = 16.3 Hz, 1H), 3.82 (t, J = 6.9 Hz, 2H), 3.55 (t, J = 6.0 Hz, 2H), 2.93–2.81 (m, 2H), 2.75–2.54 (m, 1H), 2.40 (t, J = 7.2 Hz, 2H), 2.12–2.00 (m, 1H), 1.90 (dp, J = 22.2, 6.9 Hz, 4H), 1.52 (t, J = 7.5 Hz, 2H), 1.37 (s, 3H), 0.79 (s, 3H). ^{13}C NMR (75 MHz, CD_3OD) δ 172.3, 172.1, 170.1, 169.0, 167.9, 166.5, 148.6, 148.2, 147.1, 146.9, 144.6, 142.2, 138.3, 136.9, 135.1, 134.1, 132.2, 130.9, 130.7, 127.5, 127.0, 123.7, 121.3, 120.0, 115.5, 111.2, 109.3, 108.4, 108.2, 77.8, 69.0, 63.2, 51.2, 44.4, 38.8, 33.1, 31.1, 29.3, 26.8, 25.3, 24.2, 21.6. LC-MS Rt: 8.768 min, purity 96.6 %, MS: 883.4. HRMS(ESI) m/z $[M+H]^+$ calcd for $[C_{47}H_{51}N_{10}O_8]^+$ 883.3886, found 883.3848; $[M+Na]^+$ calcd for $[C_{47}H_{50}N_{10}O_8Na]^+$ 905.3705, found 905.3672.

4.1.23. 4-((5-(4-((1-(2-(2-(2-((2-(2,6-Dioxopiperidin-3-yl)-1,3-dioxoisoindolin-4-yl)amino)ethoxy)ethoxy)ethyl)-1H-1,2,3-triazol-4-yl)methoxy)butanamido)-3,3-dimethyl-2-(pyridin-3-yl)indolin-1-yl)methyl)-N-hydroxybenzamide (5d)

Compound **5d** was obtained from compound **23d** (24 mg, 0.02 mmol) by following General Procedure B. Purification by column chromatography on silica gel (30:1 to 5:1 DCM/MeOH) afforded the title compound as an amorphous yellow solid (28 % yield). ESI-MS *m/z*: 943 $[M+H]^+$. ^{1}H NMR (300 MHz, CD_3OD) δ 8.74 (d, $J = 8.5$ Hz, 1H), 8.50 (s, 2H), 7.99 (s, 1H), 7.88 (s, 1H), 7.82–7.64 (m, 3H), 7.56 (d, $J = 7.3$ Hz, 1H), 7.44–7.27 (m, 4H), 7.09 (dd, $J = 8.3$, 2.1 Hz, 1H), 6.43 (d, $J = 8.4$ Hz, 1H), 5.18 (dd, $J = 12.9$, 5.3 Hz, 1H), 4.57–4.47 (m, 4H), 4.46–4.29 (m, 2H), 4.11–3.78 (m, 4H), 3.55 (d, $J = 7.4$ Hz, 9H), 2.88 (d, $J = 4.5$ Hz, 2H), 2.70 (dq, $J = 12.7$, 6.7 Hz, 1H), 2.40 (t, $J = 7.3$ Hz, 2H), 2.10 (s, 1H), 1.98–1.88 (m, 2H), 1.37 (s, 3H), 0.79 (s, 3H). ^{13}C NMR (75 MHz, CD_3OD) δ 172.3, 171.9, 169.6, 161.3, 161.1, 156.5, 148.1, 147.1, 144.4, 142.1, 138.3, 135.8, 131.0, 130.7, 127.5, 125.5, 120.0, 70.0, 67.3, 63.2, 50.0, 44.5, 39.0, 35.1, 33.5, 33.0, 31.2, 25.3. LC-MS Rt: 8.659 min, purity 95.5 %. HRMS(ESI) *m/z* $[M+H]^+$ calcd for $[C_{49}H_{55}N_{10}O_{10}]^+$ 943.4097, found 943.4057; $[M+Na]^+$ calcd for $[C_{49}H_{54}N_{10}O_{10}Na]^+$ 965.3917, found 965.3876.

4.1.24. 4-((5-(3-(2-(2,6-Dioxopiperidin-3-yl)-1,3-dioxoisoindolin-4-yl)ureido)-3,3-dimethyl-2-(pyridin-3-yl)indolin-1-yl)methyl)-N-((tetrahydro-2H-pyran-2-yl)oxy)benzamide (25)

To a solution of pomalidomide (**2**, 20 mg, 0.07 mmol) in dry THF (1 mL), 4-nitrophenylchloroformate (22 mg, 0.11 mmol) was added. The reaction mixture was refluxed for 14 h, shifting from a yellow suspension to a colorless solution. Then, it was allowed to reach rt. TEA (31 μL, 0.22 mmol) and compound **14** (35 mg, 0.07 mmol) were added and the mixture was stirred at 60 °C for 4 h. After cooling to rt, a saturated solution of NH_4Cl was added and the organic products were extracted with EtOAc (3 x 10 mL). The combined organic layers were dried over anhydrous Na_2SO_4, and the solvents were removed under reduced pressure. The crude product was used in the next step without any further purification. ESI-MS *m/z*: 793 $[M+Na]^+$.

4.1.25. 4-((5-(3-(2-(2,6-Dioxopiperidin-3-yl)-1,3-dioxoisoindolin-4-yl)ureido)-3,3-dimethyl-2-(pyridin-3-yl)indolin-1-yl)methyl)-N-hydroxybenzamide (6)

Compound **6** was obtained from compound **25** (38 mg, 0.05 mmol) by following General Procedure B. Purification by column chromatography on silica gel (30:1 to 10:1 DCM/MeOH) afforded the title compound as an amorphous yellow solid (41 % yield). ESI-MS *m/z*: 688 $[M+H]^+$, 710 $[M+Na]^+$. ^{1}H NMR (300 MHz, CD_3OD) δ 8.65 (d, $J = 8.5$ Hz, 1H), 8.49 (d, $J = 4.9$ Hz, 2H), 7.87 (s, 1H), 7.77–7.64 (m, 3H), 7.49–7.32 (m, 4H), 7.25 (s, 1H), 7.06 (dd, $J = 8.3$, 2.1 Hz, 1H), 6.49 (dd, $J = 8.4$, 3.0 Hz, 1H), 5.12 (dd, $J = 12.7$, 5.2 Hz, 1H), 4.42 (d, $J = 16.3$ Hz, 1H), 4.34 (d, $J = 1.9$ Hz, 1H), 4.06 (d, $J = 16.2$ Hz, 1H), 2.97–2.70 (m, 3H), 2.15 (s, 1H), 1.40 (d, $J = 2.2$ Hz, 3H), 0.83 (s, 3H). ^{13}C NMR (75 MHz, CD_3OD) δ 173.4, 173.2, 172.6, 170.0, 168.7, 162.1, 161.3, 146.4, 138.8, 134.4, 134.2, 132.7, 127.4, 126.9, 120.4, 116.1, 111.1, 110.0, 80.6, 55.3, 44.5, 32.2, 30.7, 22.2. LC-MS Rt: 8.738 min, purity 98.1 %, MS: 688.3 HRMS(ESI) *m/z* $[M+H]^+$ calcd for $[C_{37}H_{34}N_7O_7]^+$ 688.2514, found 688.2489.

4.2. Computational studies

4.2.1. Preparation of the models

The X-ray structures of *h*HDAC6 bound to trichostatin A (PDB id: 5EDU) [45] and of CRBN in complex with protein damaged DNA–binding protein 1 (DDB1) and lenalidomide (PDB id: 4TZ4) [46] were used to model the ternary complexes HDAC6:PROTAC:CRBN. In the case of *h*HDAC6, residues 111 to 478 were removed, and the subsequent molecular modelling studies were performed on the catalytic domain 2, comprising residues 479 to 835. The resulting model was refined using the Protein Preparation Wizard tool [53,54] within the Schrödinger 2024-2 suite. Hydrogen atoms were added to the structure, and the protonation state of ionizable amino acids was attributed to be consistent with physiological pH. Histidine and aspartate residues also engaged in the Zn^{2+} chelation (i.e., His614, Asp612 and Asp705) were modelled in their neutral and negatively charged form, respectively. In this step, following the default procedure of the Protein Preparation Wizard, coordination bonds were modelled by creating zero-order bonds between the atoms of the protein and ligand and the Zn^{2+}. The model was subjected to minimization performed with the OPLS4 force field [55], during which only the hydrogen atoms were left unrestrained. A second minimization run was finally performed, restraining the position of the system heavy atoms to a RMSD of 0.1 Å. In the case of CRBN, the residues of chain A (corresponding to DDB1) were removed, exclusively retaining the entire structure of CRBN (chain C). The structure of CRBN was then refined using the Protein Preparation Wizard tool, following the same protocol described above.

The structure of **1** was built in Maestro 14.1 [56], and prepared using the Ligprep tool, modelling the hydroxamic acid group in its neutral form. Compound **1** was then docked within the *h*HDAC6 binding site using Glide 10.3 [57–59]. The docking grid was centred on the geometry of the co-crystallized ligand trichostatin A, setting the inner and outer box grid dimensions to 12 and 32 Å. During the docking, a metal-coordination restraint between the Zn^{2+} ion and the hydroxamic group of **1** was applied. The docking studies were conducted using the standard precision (SP) mode, and the resulting poses were ranked according to their Emodel value. The top-ranked docking pose was energy-minimized using Macromodel 14.4 [60] using the OPLS4 force field in an implicit water model, applying the Polak-Ribiere conjugate gradient method, setting the energy gradient convergence to 0.05 kcal mol^{-1} $Å^{-2}$. During the minimization, the backbone was fixed.

The resulting model was used to build each PROTAC (**5a** and **6**) on the geometry of the common HDAC-binder adopted from compound **1**. Each *h*HDAC6-PROTAC complex was energy-minimized using Macromodel 14.4 using the OPLS4 force field in an implicit water model, applying the Polak-Ribiere conjugate gradient method, setting the energy gradient convergence to 0.05 kcal mol^{-1} $Å^{-2}$. During the minimization, the heavy atoms of the backbone were fixed, while the heavy atoms of the common HDAC-binder portion were restrained to the coordinates of the energy-minimized docking pose of **1**. The resulting geometries were submitted to metadynamics simulations to explore the conformational space of the linker of the PROTACs.

4.2.2. Metadynamics simulations on HDAC6-PROTACs complexes

Metadynamics simulations were performed using Desmond 7.8 [61] within the Schrodinger suite on the *h*HDAC6-PROTACs complexes to explore the conformational space of the linker and thalidomide portions of each ligand. Each *h*HDAC6-PROTAC complex was solvated by approximately 14000 TIP3P water molecules and neutralized by adding 3 Na^+ counterions. Following an equilibration step, during which the temperature of the system was raised up to 300K, and restraints on the protein and ligand were progressively reduced, for each system a 200 ns-long metadynamics simulation was performed in NVT conditions. During the metadynamics simulations, hydrogen atoms were constrained by applying the M-SHAKE algorithm, and short-range and electrostatic interactions were treated using the Particle-Mesh-Ewald method. A RESPA integrator was used with a time-step of 2 fs, and long-range interactions were computed every 6 fs. The backbone and the heavy atoms of the common HDAC binder portion were restrained to their crystallographic coordinates by applying a harmonic restraint of 0.5 kcal mol^{-1} $Å^{-2}$. To explore the conformational space of the linker and thalidomide fragment of the PROTACs, we devised different collective variables (CVs). In the case of **5a**, we selected five CVs: the dihedral angles describing the rotation along the bonds between the HDAC binder and the amidic linker and of the last two bonds connecting the triazole ring to the thalidomide portion, and the distances between

the center of mass of the triazole ring and the amide group of the linker and the phthalimide ring. The width of the gaussians was set to 2° and 0.2 Å, while the height and deposition interval were set to 0.1 kcal mol^{-1} and 10 ps. In the case of **6**, which was characterized by a more rigid structure, we used as CV the dihedral angle describing the rotation along the bond between the ureidic linker and the HDAC binder. The width of the gaussians was set to 2°, while the height and deposition interval were set to 0.1 kcal mol^{-1} and 10 ps. To avoid conformations in which the thalidomide portion was stuck on the surface of HDAC6, a biasing potential was also added on the number of contacts between the thalidomide and the protein. A cluster analysis was then performed on the collected trajectories upon alignment on the X-ray structure of *h*HDAC6, in order to identify different conformers. For each PROTAC, 2000 snapshots (one every 100 ps) were extracted from the metadynamics simulation trajectory and aligned on the X-ray structure of *h*HDAC6. The 2000 snapshots were then clustered using a built-in tool of the Schrödinger 2024-2 suite according to the torsional RMSD computed for the dihedrals of the linker. The average linkage method was applied for hierarchical clustering, and the Kelley index [62] was used as criterion to select the optimal number of clusters. This procedure allowed to identify 38 and 12 clusters of conformers for **5a** and **6**, respectively. The geometries of clusters centroids were used for subsequent molecular modelling studies.

4.2.3. Generation of the hHDAC6:PROTAC:CRBN ternary complexes by structure superposition

In the case of **5a**, 14 conformers out of 38 were characterized by an extended linker conformation, in which the CRBN-binding fragment was projected far from the surface of *h*HDAC6. This latter set of conformers was further analyzed to identify and select *h*HDAC6-**5a** complexes in which none of the heavy atoms of the thalidomide fragment of the PROTAC would contact any protein residue within a sphere of 8 Å. Three conformers matched this criterion, and were selected as starting geometries to build the *h*HDAC6:**5a**:CRBN ternary complexes. To assess the suitability of the complex formation, without any unfavorable steric clash (i.e. with no backbone overlapping), we adopted a strategy already described in the literature [63,64], and built the ternary complexes by superposing the prepared coordinates of CRBN co-crystallized with lenalidomide on the corresponding fragment of each *h*HDAC6-**5a** conformer. In the case of **6**, characterized by a rigid ureidic linker, only 2 out of 12 conformations projected the thalidomide portions towards the solvent while maintaining a planar geometry for the urea spacer. These two configurations (i.e., in which the ureidic linker was 180°-rotated) were selected to evaluate the feasibility of the ternary complex formation. Also in this case, ternary complexes were built by superposing the prepared coordinates of CRBN co-crystallized with lenalidomide on the corresponding fragment of each *h*HDAC6-**6** conformer, as done for compound **5a.**

4.2.4. Protein-protein docking protocol

The protein-protein docking procedure was carried out using the PIPER [65] program within the Schrödinger 2024-2 suite. The crystallographic geometries of the CRBN-lenalidomide complex (*ligand*) were rigidly docked on the surface of the complex *h*HDAC6-**1** (*receptor*), sampling different orientations of the *ligand* translated on the surface of the receptor to find the best docking poses. At this stage, constraints were set to avoid docking poses in which the interface was mediated by regions that, being situated at a distance of at least 20 Å from the binding sites of the two proteins, would unlikely be involved in the formation of a ternary complex *h*HDAC6:PROTAC:CRBN. The protein-protein docking poses were ranked according to their PIPER pose energy score, and the first 1000 solutions were retained. By adapting a recently described computational protocol [66], the binding modes obtained through the protein-protein docking process were then filtered according to the possibility to match the position of the lenalidomide with the thalidomide portion in any of the conformations identified through metadynamics simulations of the PROTACs bound to HDAC6. Specifically, the first 1000 protein-protein docking poses were re-ranked according to the RMSD values (i.e., the lowest value being the best) between the heavy atoms of lenalidomide co-crystallized within CRBN and the corresponding atoms of the thalidomide scaffold in the conformations identified through the metadynamics simulation, after superposition on the backbone of the *h*HDAC6 structure employed for the protein-protein docking. The binding modes satisfying the acceptance criterion were further optimized to remove side chains clashes and to optimize the PROTACs geometries within the binding site at the interface of the two proteins. Side chains of residues showing a steric clash were removed and re-built using the Protein Preparation Wizard tool. The resulting complexes were then energy-minimized with Macromodel 14.4, using the OPLS4 force field in an implicit water model, applying the Polak-Ribiere conjugate gradient method, setting the energy gradient convergence to 0.05 kcal mol^{-1} $Å^{-2}$. During the minimization, the heavy atoms of *h*HDAC6 and CRBN were fixed, while all the atoms of the PROTACs were free to move.

4.2.5. Molecular dynamics simulations on the HDAC6:PROTAC:CRBN ternary complexes

MD simulations were performed to assess the reliability of the modelled HDAC6:PROTAC:CRBN complexes, i.e. the ability of the PROTACs to maintain the pharmacophoric interactions of the HDAC and CRBN binders within the ternary complex. Each ternary complex was solvated by approximately 37000 TIP3P water molecules and neutralized by adding 4 Na^+ counterions. An initial equilibration was performed, during which the temperature of the system was raised up to 300 K, while maintaining restraints on the heavy atoms of the proteins and of the PROTAC. Restraints on the heavy atoms of the PROTAC, followed by CRBN and finally by HDAC6, were progressively removed. During this step, restraints on the intramolecular H-bonds of the backbone of the proteins and on the H-bonds between the PROTAC and HDAC6 and CRBN were also applied and gradually removed, in order to maintain the protein structure as close as possible to the crystallographic structure. MD simulations were finally performed in NVT conditions without any restraint on the system for 400 ns.

4.3. Biological assays

4.3.1. A549 lung cancer cells experiments

4.3.1.1. Cell culture. A549 (CCL-185) cell lines were purchased from ATCC (Milan, Italy). Cells were grown in Dulbecco's Modified Eagle's Medium (DMEM; Euroclone, Milan, Italy, #ECB7501L) (DMEM; Euroclone, Milan, Italy, #ECB7501L), supplemented with 10 % heat-inactivated fetal bovine serum (FBS; Sigma-Aldrich, St. Louis, USA, #F7524), antimicrobials (100 U/mL penicillin, 100 μg/mL streptomycin (Euroclone, ECB3001D), 250 ng/mL amphotericin B (Euroclone, ECM0009D) and were cultivated at 37 °C with 5 % CO_2 and checked for mycoplasma contamination using EZ-PCR Mycoplasma Test Kit (Biological Industries, Cromwell, CT, USA, #20-700-20).

4.3.1.2. Cell viability assay. A549 cell viability was performed using thiazolyl blue tetrazolium bromide (3-(4,5-dimethylthiazol-2-yl)-2,5-diphenyltetrazolium bromide) (MTT; Sigma-Aldrich, Schnelldorf, Germany, #57360-69-7), following the manufacturer's instructions. Cells were seeded at a density of 7×10^3 cells/well in a 96-well plate, the next day, they were induced with compounds. All the compounds were used at final concentrations of 1 μM, 5 μM, 10 μM, 25 μM, 50 μM for 24, 48 and 72 h. SAHA was used at 5 μM, TubA and Pomalidomide at 10 μM. Experiments were performed in triplicates and repeated three times. Absorbance values were read at a wavelength of 570 nm detected by TECAN M200 reader (Tecan, Männedorf, Switzerland).

4.3.1.3. Total protein extraction. Following the treatment with indicated compound at 10 or 1 μM, cell pellets was collected and suspended in lysis buffer (50 mmol/L Tris–HCl pH 7.4, 150 mmol/L NaCl, 1 % NP40, 10 mmol/L NaF, 1 mmol/L PMSF, and protease inhibitor cocktail). Next, the samples were vortexed in three cycles interspersed by 2 min and then the lysis reaction was carried out for 15 min at 4 °C, samples were centrifuged at 13,000 rpm for 30 min at 4 °C, and protein concentration was determined with Bradford assay (Bio-Rad Protein Assay Dye Reagent Concentrate, Bio-Rad, Hercules, CA, USA, #5000006).

4.3.1.4. Western blot analysis. A total of 30 μg from total extract was loaded on 10 % polyacrylamide gel and electro-blotted on nitrocellulose membranes. Immunoreactive signals were detected with a horseradish peroxidase-conjugated secondary antibody (Bio-Rad, anti-rabbit, #1705046, anti-mouse, #1706516) and chemiluminescence signals were developed upon ECL (Clarity Western ECL Substrate, 500 mL #1705061). Primary antibodies: HDAC6 (#7558), Acetylated-tubulin (#5335), and GAPDH (#D16H11), all purchased from Cell Signaling Technology (Danvers, MA, USA). All antibodies were used according to the manufacturer's instructions. Semi-quantitative analysis was performed using ImageJ software (version 1.44).

4.3.2. IMR-90 lung fibroblasts experiments

4.3.2.1. Cell culture. The IMR-90 Cell Line (CCL-189TM) were purchased from the American Type Culture Collection (ATCC, Manassas, VA, USA). This cell line comprises fibroblasts isolated from normal lung tissue derived from a 16-week-old female. IMR-90 were cultured at 37 °C in a 5 % CO_2 incubator in T-75 flasks. Confluent cells at passages 1–7 were used for the experiments. Culture medium was Advanced MEM (Minimum Essential Medium) (Gibco, Grand Island, NY, USA) added with 2 mM glutamine, 100 U/L penicillin and 0,1 mg/L streptomycin (Sigma Aldrich, St. Louis, MO, USA) with 10 % Defined Fetal Bovine Serum (FBS) (HyClone, South Logan, UT, USA). The control of mycoplasma was routinely performed, starting from frozen vials. TGF-β1 (T7039-2UG, Sigma Aldrich, St. Louis, MO, USA) was purchased as powder. 2 μg of TGF-β1 were resuspended in sterile H_2O milliQ to reach a stock concentration of 10 μg/mL. Stocks were stored at −20 °C while waiting to be diluted in the experiments. Cells were photographed during the experiments by using a microscope (Nikon Eclipse E400, Tallahassee, FL, USA).

4.3.2.2. Western blot. To study HDAC6 degradation, IMR-90 cells were seeded in 60 mm Petri plates in Advanced MEM with 10 % FBS. The cells were incubated for 24 h at 37 °C and 5 % CO_2 to allow adherence and then treated with two concentrations (0.1 and 1 μM) of the PROTACs **5a** and **5c** in a range of h from 6 to 24 h in medium with 2 % FBS. To study HDAC6 degradation in the presence of proteasome and neddylation inhibitors, cells were seeded in n 60 mm Petri plates in Advanced MEM with 10 % FBS. After 24 h, cells were pre-treated with MG132 (0.1 μM) or MLN4924 (0.1 μM) for 30 min, followed by co-treatment with **5a** (1 μM) for 24 h in medium containing 2 % FBS. MG132 was purchased from MedChemExpress (#HY-13259) while MLN4924 was purchased from Cell Signaling (#85923). To establish the fibrosis model *in vitro*, IMR-90 cells were seeded in 60 mm Petri plates in Advanced MEM with 10 % FBS, allowed to adhere and then starved for 24 h (serum deprivation). Next the cells were co-stimulated with TGF-β1(5 ng/mL) and the compounds **5a** and **5c** (1 μM) every 24 h for a total duration of 48 h. At the end of stimulation, IMR-90 were washed 2x with cold Dulbecco's Phosphate Buffered Saline (PBS) (Merck KGaA Darmstadt, Germany) and lysed on ice with RIPA Buffer supplemented with 2 mM Na_3VO_4 and 1x Protease inhibitor cocktail for mammalian cells (Merck KGaA Darmstadt, Germany). Cell lysates were centrifuged at 16000×*g* (for 20 min at 4 °C and the supernatants were then collected. Bradford assay was used to determine the protein concentration. Proteins (50 μg/sample) were separated by polyacrylamide gel electrophoresis (Bolt 4–15 %, TGX Stain-Free, 1.0 mm, Mini-Protean Gel, 10-well, from Bio-rad, Hercules, CA, USA). Proteins were transferred onto a nitrocellulose membrane (Bio-rad, Hercules, CA, USA). Next, membranes were blocked with 5 % non-fat dried milk for 1 h at rt, and then incubated at 4 °C overnight with primary antibody including anti-HDAC6 (rabbit, Cell Signaling, mAb #7558), anti-HDAC1 (mAb, Active Motif, cat. No. 39531), anti-fibronectin (rabbit, Cell Signaling, mAb #26836), anti-αSMA (mouse, Merck KGaA, mAb, cat. No. A5228), anti-acetylated tubulin (mouse, Merck KGaA, mAb, cat. No. T7451), anti-NEDD8 (rabbit, Cell Signaling, mAb #2754), anti-GAPDH (rabbit, Cell Signaling, mAb # 5174) and anti-β-actin (mouse, mAb, cat. no. MABT825). The membranes were washed three times (with PBS and TWEEN20 0.5 %) and then incubated with secondary antibodies, HRP conjugated (anti-rabbit, 1:2500, cat. n. W401B; anti-mouse 1:2500, cat. n. W402B, both from Promega Corporation Madison, Wisconsin, USA) at rt for 1 h. At the end of incubation, membranes were washed with PBS and TWEEN20 0.5 % (Merck KGaA. (Darmstadt, Germany) three times. The analysis of protein bands was conducted using ChemiDoc XRS (Bio-Rad Laboratories, Inc. Milan, Italy) after incubating at room temperature for 2 min with an enhanced chemiluminescent substrate (Bio-Rad Laboratories, Inc. Milan, Italy). Each experiment was performed at least three times. Densitometry analysis of immunoblots was performed using Fiji software (64-bit Java 1.8.0_172). The results, presented as arbitrary density units (A.D.U.) ± SD, were normalized against total protein (when suitable) and subsequently β-actin [67].

4.3.2.3. Immunofluorescence analysis. IMR-90 were cultured on 1 cm circular glass coverslips added in the bottom of a 24 well multiplate. Next, IMR-90 were starved in serum-free medium for 24 h, and then treated with TGF-β1 (5 ng/mL) and **5a** and **5c** (1 μM) every 24 h for a total duration of 48 h. Immunofluorescence analysis was performed as previously reported using antibody anti-αSMA (mouse, Merck KGaA, mAb, cat. No. A5228) and DAPI to counterstain nuclei. Images were taken using a confocal microscope (Zeiss LSM700; Zeiss GmbH, Oberkochen, Germany).

4.4. Human HDAC inhibition assays

For the evaluation of their inhibitory activity, different concentrations of the compounds were incubated in a low-binding black 96-well plate with 30 ng of human recombinant HDAC6 (BPS Bioscience, San Diego, CA, USA; Cat. # 50056), human recombinant HDAC1 (BPS Bioscience; Cat. # 50051), human recombinant HDAC8 (BPS Bioscience; Cat. # 50008), or 500 ng of human recombinant HDAC10 (BPS Bioscience; Cat. # 50060) in an assay buffer composed of 25 mM Tris/HCl, pH 8.0, 137 mM NaCl, 2.7 mM KCl, 1 mM $MgCl_2$, and 0.1 mg/mL bovine serum albumin for 30 min at 37 °C. At the end of the incubation, the deacetylation reaction was initiated by adding 200 μM of the fluorogenic acetylated HDAC substrate 3 (BPS Bioscience; Cat. # 50037) for HDAC6, HDAC1 and HDAC10 assays, or of the fluorogenic HDAC substrate class 2A (BPS Bioscience; Cat. #50040) for HDAC8 assays. After 30 min at 37 °C, the reaction was stopped by the addition of an HDAC assay developer (BPS Bioscience; Cat. # 50060). Following an incubation of 15 min at RT, fluorescence was measured in an EnSight multimodal plate reader (PerkinElmer, Boston, MA, USA) with an excitation wavelength of 360 nm and an emission wavelength of 450 nm.

CRediT authorship contribution statement

Ilaria Cursaro: Investigation, Formal analysis, Data curation. **Valerio Ciccone:** Methodology, Investigation. **Valeria Tudino:** Methodology, Investigation, Formal analysis, Data curation. **Chiara Papulino:** Resources, Formal analysis, Data curation. **Laura Scalvini:**

Validation, Software. **Sandra Donnini:** Validation, Supervision. **Lucia Morbidelli:** Validation, Supervision, Software, Data curation. **Luca Bini:** Resources, Methodology, Data curation. **Claudia Landi:** Visualization, Validation. **Chiara Contri:** Investigation, Formal analysis, Data curation. **Silvia Pasquini:** Investigation, Formal analysis. **Fabrizio Vincenzi:** Formal analysis, Data curation. **Katia Varani:** Investigation, Formal analysis, Data curation. **Alessio Lodola:** Visualization, Validation, Supervision, Software, Conceptualization. **Marco Mor:** Supervision, Software, Resources, Formal analysis, Data curation. **Rosaria Benedetti:** Formal analysis, Data curation, Conceptualization. **Lucia Altucci:** Resources, Methodology, Investigation, Formal analysis. **Stefania Butini:** Resources, Project administration, Methodology, Investigation. **Gabriele Carullo:** Methodology, Conceptualization. **Sandra Gemma:** Formal analysis, Data curation, Conceptualization. **Giuseppe Campiani:** Project administration, Funding acquisition, Formal analysis, Data curation, Conceptualization.

Declaration of competing interest

The authors declare that they have no known competing financial interests or personal relationships that could have appeared to influence the work reported in this paper.

Acknowledgments

Giuseppe Campiani and Stefania Butini thank Next Generation EU – National Recovery and Resilience Plan (NRRP) – Mission 4 Component 2 Investment 1.4 – Italian Ministry of University and Research (MUR) Project Code ECS_00000017 MUR Directoral Decree n.1055, June 23, 2022, CUP B83C22003930001, "Tuscany Health Ecosystem – THE" - Spokes 7–8. Giuseppe Campiani, Stefania Butini, Luca Bini and Claudia Landi thank Regione Toscana IT for the grant Bando Ricerca Salute 2018-Regione Toscana – HIDE-IPF, "Epigenetic and proteomic approaches towards innovative targeted therapies for IPF". Rosaria Benedetti thanks PNRR-MAD-2022–12376723; PNRR-CN3, National Centre for Gene Therapy and Drugs Based on RNA Technology, cod: CN000000041. Lucia Altucci thank EPI- MET Fondo Crescita Sostenibile—Accordi per l'Innovazione di cui al D.M. December 31, 2021 e D.D. March 18, 2022 Progetto posizione n. 34; n. progetto F/310034/03/X56. PRIN P2022F3YRF. Chiara Papulino thank project n. PNC0000003—AdvaNced Technologies for Human-centrEd Medicine (project acronym: ANTHEM). Rosaria Benedetti thanks Piano Nazionale di Ripresa e Resilienza Missione 4 - Componente 2 - Investimento 1.5 Titolo del progetto: **Umen** - Unveiling the Metabolic and Epigenetic Signature of Neuroendocrine Prostate Cancer Codice CUP B83C22003920001 and Programma di Ricerca del Tuscany Health Ecosystem, a valere sulle risorse del Piano Nazionale Ripresa e Resilienza (PNRR) missione 4, "Istruzione e Ricerca" - componente 2, "Dalla Ricerca all'Impresa" - linea di investimento 1.5, finanziato dall'Unione Europea – NextGenerationEU "MEDUSA" - CUP B63C22002450007. Heal Italia – Health extended alliance for innovative therapies, advanced lab-research, and integrated approaches of precision medicine" – PE_00000019 Spoke 3: Università degli Studi di Palermo – CUP B73C22001250006 Prediction models - Modelli avanzati di predizione per la prognosi e la risposta terapeutica DARIA. This research benefits from the High-Performance Computing facility of the University of Parma, Italy (HPC.unipr.it). This work has been carried out in the frame of the ALIFAR project, funded by the Italian Ministry of University through the program 'Dipartimenti di Eccellenza 2023–2027'.

Appendix. A Supplementary data

Supplementary data to this article can be found online at https://doi.org/10.1016/j.ejmcr.2025.100276.

Abbreviations used

α-SMA: alpha-smooth muscle actin; AEC: alveolar epithelial cell; CD: catalytic domain; CRBN: cereblon; $CRL4^{CRBN}$: CUL4-DDB1-RBX1 E3 ubiquitin ligase E3 ligase complex; DIPEA: *N*,*N*-diisopropylethylamine; DMAP: 4-dimethylaminopyridine; DMF: *N*,*N*-dimethylformammide; DMSO: dimethyl sulfoxide; ECM: extracellular matrix; EDC-HCl: *N*-(3-Dimethylaminopropyl)-*N*′-ethylcarbodiimide hydrochloride; EMT: epithelial-mesenchymal transition; EtOAc: ethyl acetate; EtOH: ethanol; HDAC: histone deacetylase; IPF: idiopathic pulmonary fibrosis; HATU: 1-[Bis(dimethylamino)methylene]-1H-1,2,3-triazolo[4,5-b]pyridinium 3-oxid hexafluorophosphate; HOBt: 1- hydroxybenzotriazole; MD: molecular dynamics; POI: protein of interest; PROTAC: proteolysis targeting chimera; SMAD3: mothers against decapentaplegic homolog 3; TBAI: tetrabutylammonium iodide; TEA: triethylamine; TFA: trifluoroacetic acid; TGF-β1: transforming growth factor β1; THF: tetrahydrofuran; THP: tetrahydropyran; TPD: targeted protein degradation; VHL: Von-Hippel Lindau.

Data availability

Data will be made available on request.

References

[1] S. Gandhi, R. Tonelli, M. Murray, A.V. Samarelli, P. Spagnolo, Environmental causes of idiopathic pulmonary fibrosis, Int. J. Mol. Sci. 24 (2023), https://doi.org/10.3390/ijms242216481.
[2] J.V. Pergolizzi, J.A. LeQuang, M. Varrassi, F. Breve, P. Magnusson, G. Varrassi, What do we need to know about rising rates of idiopathic pulmonary fibrosis? A narrative review and update, Adv. Ther. 40 (2023) 1334–1346, https://doi.org/10.1007/s12325-022-02395-9.
[3] A. Chakraborty, M. Mastalerz, M. Ansari, H.B. Schiller, C.A. Staab-Weijnitz, Emerging roles of airway epithelial cells in idiopathic pulmonary fibrosis, Cells 11 (2022), https://doi.org/10.3390/cells11061050.
[4] F. Bonella, P. Spagnolo, C. Ryerson, Current and future treatment landscape for idiopathic pulmonary fibrosis, Drugs (Basel) 83 (2023) 1581–1593, https://doi.org/10.1007/s40265-023-01950-0.
[5] E.H. Budi, J.R. Schaub, M. Decaris, S. Turner, R. Derynck, TGF-β as a driver of fibrosis: physiological roles and therapeutic opportunities, J. Pathol. 254 (2021) 358–373, https://doi.org/10.1002/path.5680.
[6] C. Júnior, A. Ulldemolins, M. Narciso, I. Almendros, R. Farré, D. Navajas, J. López, M. Eroles, F. Rico, N. Gavara, Multi-step extracellular matrix remodelling and stiffening in the development of idiopathic pulmonary fibrosis, Int. J. Mol. Sci. 24 (2023), https://doi.org/10.3390/ijms24021708.
[7] D.S. Glass, D. Grossfeld, H.A. Renna, P. Agarwala, P. Spiegler, J. DeLeon, A. B. Reiss, Idiopathic pulmonary fibrosis: current and future treatment, Clinical Respiratory Journal 16 (2022) 84–96, https://doi.org/10.1111/crj.13466.
[8] I.V. Yang, D.A. Schwartz, Epigenetics of idiopathic pulmonary fibrosis, Transl. Res. 165 (2015) 48–60, https://doi.org/10.1016/j.trsl.2014.03.011.
[9] C. Tirelli, C. Pesenti, M. Miozzo, M. Mondoni, L. Fontana, S. Centanni, The genetic and epigenetic footprint in idiopathic pulmonary fibrosis and familial pulmonary fibrosis: a state-of-the-art review, Diagnostics 12 (2022), https://doi.org/10.3390/diagnostics12123107.
[10] M. Korfei, P. Mahavadi, A. Guenther, Targeting histone deacetylases in idiopathic pulmonary fibrosis: a future therapeutic option, Cells 11 (2022), https://doi.org/10.3390/cells11101626.
[11] X. Lyu, M. Hu, J. Peng, X. Zhang, Y.Y. Sanders, HDAC inhibitors as antifibrotic drugs in cardiac and pulmonary fibrosis, Ther Adv Chronic Dis 10 (2019), https://doi.org/10.1177/2040622319862697.
[12] F. Conforti, E.R. Davies, C.J. Calderwood, T.H. Thatcher, M.G. Jones, D.E. Smart, S. Mahajan, A. Alzetani, T. Havelock, T.M. Maher, P.L. Molyneaux, A.J. Thorley, T. D. Tetley, J.A. Warner, G. Packham, A. Ganesan, P.J. Skipp, B.J. Marshall, L. Richeldi, P.J. Sime, K.M.A. O'reilly, D.E. Davies, The histone deacetylase inhibitor. Romidepsin, as a Potential Treatment for Pulmonary Fibrosis, 2017. www.impactjournals.com/oncotarget.
[13] K. Van Beneden, I. Mannaerts, M. Pauwels, C. Van den Branden, L.A. van Grunsven, HDAC inhibitors in experimental liver and kidney fibrosis, Fibrogenesis Tissue Repair 6 (2013), https://doi.org/10.1186/1755-1536-6-1.
[14] S. Yoon, G. Kang, G.H. Eom, Hdac inhibitors: therapeutic potential in fibrosis-associated human diseases, Int. J. Mol. Sci. 20 (2019), https://doi.org/10.3390/ijms20061329.
[15] A. Fontana, I. Cursaro, G. Carullo, S. Gemma, S. Butini, G. Campiani, A therapeutic perspective of HDAC8 in different diseases: an overview of selective inhibitors, Int. J. Mol. Sci. 23 (2022), https://doi.org/10.3390/ijms231710014.
[16] H. Yu, S. Liu, S. Wang, X. Gu, A narrative review of the role of HDAC6 in idiopathic pulmonary fibrosis, J. Thorac. Dis. 16 (2024) 688–695, https://doi.org/10.21037/jtd-23-1183.

[17] B. Shan, T.P. Yao, H.T. Nguyen, Y. Zhuo, D.R. Levy, R.C. Klingsberg, H. Tao, M. L. Palmer, K.N. Holder, J.A. Lasky, Requirement of HDAC6 for transforming growth factor-β1-induced epithelial-mesenchymal transition, J. Biol. Chem. 283 (2008) 21065–21073, https://doi.org/10.1074/jbc.M802786200.
[18] G. Campiani, C. Cavella, J.D. Osko, M. Brindisi, N. Relitti, S. Brogi, A.P. Saraswati, S. Federico, G. Chemi, S. Maramai, G. Carullo, B. Jaeger, A. Carleo, R. Benedetti, F. Sarno, S. Lamponi, P. Rottoli, E. Bargagli, C. Bertucci, D. Tedesco, D. Herp, J. Senger, G. Ruberti, F. Saccoccia, S. Saponara, B. Gorelli, M. Valoti, B. Kennedy, H. Sundaramurthi, S. Butini, M. Jung, K.M. Roach, L. Altucci, P. Bradding, D. W. Christianson, S. Gemma, A. Prasse, Harnessing the role of HDAC6 in idiopathic pulmonary fibrosis: design, synthesis, structural analysis, and biological evaluation of potent inhibitors, J. Med. Chem. 64 (2021) 9960–9988, https://doi.org/10.1021/acs.jmedchem.1c00184.
[19] M. Korfei, S. Skwarna, I. Henneke, B.A. MacKenzie, O. Klymenko, S. Saito, C. Ruppert, D. Von Der Beck, P. Mahavadi, W. Klepetko, S. Bellusci, B. Crestani, S. S. Pullamsetti, L. Fink, W. Seeger, O.H. Krämer, A. Guenther, Aberrant expression and activity of histone deacetylases in sporadic idiopathic pulmonary fibrosis, Thorax 70 (2015) 1022–1032, https://doi.org/10.1136/thoraxjnl-2014-206411.
[20] S. Saito, Y. Zhuang, B. Shan, S. Danchuk, F. Luo, M. Korfei, A. Guenther, J.A. Lasky, Tubastatin ameliorates pulmonary fibrosis by targeting the TGFβ-PI3K-Akt pathway, PLoS One 12 (2017), https://doi.org/10.1371/journal.pone.0186615.
[21] A. Papa, I. Cursaro, L. Pozzetti, C. Contri, M. Cappello, S. Pasquini, G. Carullo, A. Ramunno, S. Gemma, K. Varani, S. Butini, G. Campiani, F. Vincenzi, Pioneering first-in-class FAAH-HDAC inhibitors as potential multitarget neuroprotective agents, Arch Pharm (Weinheim) 356 (2023), https://doi.org/10.1002/ardp.202300410.
[22] M. Brindisi, C. Cavella, S. Brogi, A. Nebbioso, J. Senger, S. Maramai, A. Ciotta, C. Iside, S. Butini, S. Lamponi, E. Novellino, L. Altucci, M. Jung, G. Campiani, S. Gemma, Phenylpyrrole-based hdac inhibitors: synthesis, molecular modeling and biological studies, Future Med. Chem. 8 (2016) 1573–1587, https://doi.org/10.4155/fmc-2016-0068.
[23] A.P. Saraswati, N. Relitti, M. Brindisi, J.D. Osko, G. Chemi, S. Federico, A. Grillo, S. Brogi, N.H. McCabe, R.C. Turkington, O. Ibrahim, J. O'Sullivan, S. Lamponi, M. Ghanim, V.P. Kelly, D. Zisterer, R. Amet, P. Hannon Barroeta, F. Vanni, C. Ulivieri, D. Herp, F. Sarno, A. Di Costanzo, F. Saccoccia, G. Ruberti, M. Jung, L. Altucci, S. Gemma, S. Butini, D.W. Christianson, G. Campiani, Spiroindoline-capped selective HDAC6 inhibitors: design, synthesis, structural analysis, and biological evaluation, ACS Med. Chem. Lett. 11 (2020) 2268–2276, https://doi.org/10.1021/acsmedchemlett.0c00395.
[24] N. Relitti, A.P. Saraswati, G. Chemi, M. Brindisi, S. Brogi, D. Herp, K. Schmidtkunz, F. Saccoccia, G. Ruberti, C. Ulivieri, F. Vanni, F. Sarno, L. Altucci, S. Lamponi, M. Jung, S. Gemma, S. Butini, G. Campiani, Novel quinolone-based potent and selective HDAC6 inhibitors: synthesis, molecular modeling studies and biological investigation, Eur. J. Med. Chem. 212 (2021) 112998, https://doi.org/10.1016/j.ejmech.2020.112998.
[25] S. Federico, T. Khan, A. Fontana, S. Brogi, R. Benedetti, F. Sarno, G. Carullo, A. Pezzotta, A.P. Saraswati, E. Passaro, L. Pozzetti, A. Papa, N. Relitti, S. Gemma, S. Butini, A. Pistocchi, A. Ramunno, F. Vincenzi, K. Varani, V. Tatangelo, L. Patrussi, C.T. Baldari, S. Saponara, B. Gorelli, S. Lamponi, M. Valoti, F. Saccoccia, M. Giannaccari, G. Ruberti, D. Herp, M. Jung, L. Altucci, G. Campiani, Azetidin-2-one-based small molecules as dual hHDAC6/HDAC8 inhibitors: investigation of their mechanism of action and impact of dual inhibition profile on cell viability, Eur. J. Med. Chem. 238 (2022) 114409, https://doi.org/10.1016/j.ejmech.2022.114409.
[26] G. Carullo, S. Rossi, V. Giudice, A. Pezzotta, U. Chianese, P. Scala, S. Carbone, A. Fontana, G. Panzeca, S. Pasquini, C. Contri, S. Gemma, A. Ramunno, S. Saponara, F. Galvani, A. Lodola, M. Mor, R. Benedetti, C. Selleri, K. Varani, S. Butini, L. Altucci, F. Vincenzi, A. Pistocchi, G. Campiani, Development of epigenetic modifiers with therapeutic potential in FMS-related tyrosine kinase 3/internal tandem duplication (FLT3/ITD) acute myeloid leukemia and other blood malignancies, ACS Pharmacol. Transl. Sci. 7 (2024) 2125–2142, https://doi.org/10.1021/acsptsci.4c00208.
[27] S. Rossi, V. Tatangelo, M. Dichiara, S. Butini, S. Gemma, S. Brogi, S. Pasquini, M. Cappello, F. Vincenzi, K. Varani, L. Lopresti, M. Malchiodi, C. Carrara, A. Gozzetti, M. Bocchia, G. Marotta, L. Patrussi, G. Carullo, C.T. Baldari, G. Campiani, A novel potent class I HDAC inhibitor reverses the STAT4/p66Shc apoptotic defect in B cells from chronic lymphocytic leukemia patients, Biomed. Pharmacother. 174 (2024) 116537, https://doi.org/10.1016/j.biopha.2024.116537.
[28] G. Carullo, N. Orsini, I. Piano, L. Pozzetti, A. Papa, A. Fontana, D. Napoli, F. Corsi, B. Di Marco, A. Galante, L. Marotta, G. Panzeca, J. O'Brien, A.G. Sanchez, H. Doherty, N. Mahon, L. Clarke, C. Contri, S. Pasquini, B. Gorelli, S. Saponara, M. Valoti, F. Vincenzi, K. Varani, A. Ramunno, S. Brogi, S. Butini, S. Gemma, B. N. Kennedy, C. Gargini, E. Strettoi, G. Campiani, Targeting relevant HDACs to support the survival of cone photoreceptors in inherited retinal diseases: identification of a potent pharmacological tool with in vitro and in vivo efficacy, J. Med. Chem. 67 (2024) 14946–14973, https://doi.org/10.1021/acs.jmedchem.4c00477.
[29] A. Fontana, L. Bergantini, G. Carullo, L. Scalvini, M. D'Alessandro, C. Papulino, P. Cameli, S. Gangi, F. Vincenzi, K. Varani, C. Contri, S. Pasquini, A. Pistocchi, A. Pezzotta, S. Carbone, S. Saponara, S. Gemma, L. Altucci, R. Benedetti, A. Lodola, M. Mor, E. Bargagli, S. Butini, G. Campiani, Spirotetrahydroisoquinoline-based histone deacetylase inhibitors as new antifibrotic agents: biological evaluation in human fibroblasts from bronchoalveolar lavages of idiopathic pulmonary fibrosis patients, ACS Pharmacol. Transl. Sci. (2024), https://doi.org/10.1021/acsptsci.4c00456.
[30] T.C.S. Ho, A.H.Y. Chan, A. Ganesan, Thirty years of HDAC inhibitors: 2020 insight and hindsight, J. Med. Chem. 63 (2020) 12460–12484, https://doi.org/10.1021/acs.jmedchem.0c00830.
[31] Y. Zhu, M. Feng, B. Wang, Y. Zheng, D. Jiang, L. Zhao, M.A.A. Mamun, H. Kang, H. Nie, X. Zhang, N. Guo, S. Qin, N. Wang, H. Liu, Y. Gao, New insights into the non-enzymatic function of HDAC6, Biomed. Pharmacother. 161 (2023), https://doi.org/10.1016/j.biopha.2023.114438.
[32] M. Békés, D.R. Langley, C.M. Crews, PROTAC targeted protein degraders: the past is prologue, Nat. Rev. Drug Discov. 21 (2022) 181–200, https://doi.org/10.1038/s41573-021-00371-6.
[33] X. Li, W. Pu, Q. Zheng, M. Ai, S. Chen, Y. Peng, Proteolysis-targeting chimeras (PROTACs) in cancer therapy, Mol. Cancer 21 (2022), https://doi.org/10.1186/s12943-021-01434-3.
[34] K. Yang, H. Wu, Z. Zhang, E.D. Leisten, X. Nie, B. Liu, Z. Wen, J. Zhang, M. D. Cunningham, W. Tang, Development of selective histone deacetylase 6 (HDAC6) degraders recruiting Von hippel–lindau (VHL) E3 ubiquitin ligase, ACS Med. Chem. Lett. 11 (2020) 575–581, https://doi.org/10.1021/acsmedchemlett.0c00046.
[35] K. Yang, Y. Song, H. Xie, H. Wu, Y.-T. Wu, E.D. Leisten, W. Tang, Development of the first small molecule histone deacetylase 6 (HDAC6) degraders, Bioorg Med Chem Lett 28 (2018) 2493–2497, https://doi.org/10.1016/j.bmcl.2018.05.057.
[36] H. Wu, K. Yang, Z. Zhang, E.D. Leisten, Z. Li, H. Xie, J. Liu, K.A. Smith, Z. Novakova, C. Barinka, W. Tang, Development of multifunctional histone deacetylase 6 degraders with potent antimyeloma activity, J. Med. Chem. 62 (2019) 7042–7057, https://doi.org/10.1021/acs.jmedchem.9b00516.
[37] Z. An, W. Lv, S. Su, W. Wu, Y. Rao, Developing potent PROTACs tools for selective degradation of HDAC6 protein, Protein Cell 10 (2019) 606–609, https://doi.org/10.1007/s13238-018-0602-z.
[38] L. Sinatra, J. Yang, J. Schliehe-Diecks, N. Dienstbier, M. Vogt, P. Gebing, L. M. Bachmann, M. Sönnichsen, T. Lenz, K. Stühler, A. Schöler, A. Borkhardt, S. Bhatia, F.K. Hansen, Solid-phase synthesis of cereblon-recruiting selective histone deacetylase 6 degraders (HDAC6 PROTACs) with antileukemic activity, J. Med. Chem. 65 (2022) 16860–16878, https://doi.org/10.1021/acs.jmedchem.2c01659.
[39] H. Yang, W. Lv, M. He, H. Deng, H. Li, W. Wu, Y. Rao, Plasticity in designing PROTACs for selective and potent degradation of HDAC6, Chemical Communications 55 (2019) 14848–14851, https://doi.org/10.1039/C9CC08509B.
[40] H.K. Garcha, O.O. Olaoye, A. Sedighi, D. Pölöske, P. Hariri, W. Yu, D.I. Abdallah, R. Moriggl, E.D. de Araujo, P.T. Gunning, Monoselective histone deacetylase 6 PROTAC degrader shows in vivo tractability, J. Med. Chem. (2025), https://doi.org/10.1021/acs.jmedchem.4c02021.
[41] J. Yang, Y. Ruan, D. Wang, J. Fan, N. Luo, H. Chen, X. Li, W. Chen, X. Wang, VHL-recruiting PROTAC attenuates renal fibrosis and preserves renal function via simultaneous degradation of Smad3 and stabilization of HIF-2α, Cell Biosci. 12 (2022) https://doi.org/10.1186/s13578-022-00936-x.
[42] F. Wang, Y. Zhan, M. Li, L. Wang, A. Zheng, C. Liu, H. Wang, T. Wang, Cell-permeable PROTAC degraders against KEAP1 efficiently suppress hepatic stellate cell activation through the antioxidant and anti-inflammatory pathway, ACS Pharmacol. Transl. Sci. 6 (2023) 76–87, https://doi.org/10.1021/acsptsci.2c00165.
[43] E. Sjöstedt, W. Zhong, L. Fagerberg, M. Karlsson, N. Mitsios, C. Adori, P. Oksvold, F. Edfors, A. Limiszewska, F. Hikmet, J. Huang, Y. Du, L. Lin, Z. Dong, L. Yang, X. Liu, H. Jiang, X. Xu, J. Wang, H. Yang, L. Bolund, A. Mardinoglu, C. Zhang, K. von Feilitzen, C. Lindskog, F. Pontén, Y. Luo, T. Hökfelt, M. Uhlén, J. Mulder, An atlas of the protein-coding genes in the human, pig, and mouse brain, Science (1979) 367, https://doi.org/10.1126/science.aay5947, 2020.
[44] J.W. Lee, S.I. Jun, K. Kim, An efficient and practical method for the synthesis of mono-N-protected α,ω-diaminoalkanes, Tetrahedron Lett. 42 (2001) 2709–2711, https://doi.org/10.1016/S0040-4039(01)00282-9.
[45] Y. Hai, D.W. Christianson, Histone deacetylase 6 structure and molecular basis of catalysis and inhibition, Nat. Chem. Biol. 12 (2016) 741–747, https://doi.org/10.1038/nchembio.2134.
[46] P.P. Chamberlain, A. Lopez-Girona, K. Miller, G. Carmel, B. Pagarigan, B. Chie-Leon, E. Rychak, L.G. Corral, Y.J. Ren, M. Wang, M. Riley, S.L. Delker, T. Ito, H. Ando, T. Mori, Y. Hirano, H. Handa, T. Hakoshima, T.O. Daniel, B.E. Cathers, Structure of the human Cereblon–DDB1–lenalidomide complex reveals basis for responsiveness to thalidomide analogs, Nat. Struct. Mol. Biol. 21 (2014) 803–809, https://doi.org/10.1038/nsmb.2874.
[47] G.-Y. Chuang, D. Kozakov, R. Brenke, S.R. Comeau, S. Vajda, DARS (decoys as the reference state) potentials for protein-protein docking, Biophys. J. 95 (2008) 4217–4227, https://doi.org/10.1529/biophysj.108.135814.
[48] I.T. Desta, K.A. Porter, B. Xia, D. Kozakov, S. Vajda, Performance and its limits in rigid body protein-protein docking, Structure 28 (2020) 1071–1081.e3, https://doi.org/10.1016/j.str.2020.06.006.
[49] R.I. Enchev, B.A. Schulman, M. Peter, Protein neddylation: beyond cullin–RING ligases, Nat. Rev. Mol. Cell Biol. 16 (2015) 30–44, https://doi.org/10.1038/nrm3919.
[50] C.C. Maquiaveli, J.F. Lucon-Júnior, S. Brogi, G. Campiani, S. Gemma, P.C. Vieira, E.R. Silva, Verbascoside inhibits promastigote growth and arginase activity of leishmania amazonensis, J Nat Prod 79 (2016) 1459–1463, https://doi.org/10.1021/acs.jnatprod.5b00875.
[51] C. Fattorusso, S. Gemma, S. Butini, P. Huleatt, B. Catalanotti, M. Persico, M. De Angelis, I. Fiorini, V. Nacci, A. Ramunno, M. Rodriquez, G. Greco, E. Novellino, A. Bergamini, S. Marini, M. Coletta, G. Maga, S. Spadari, G. Campiani, Specific targeting highly conserved residues in the HIV-1 reverse transcriptase primer grip region. Design, synthesis, and biological evaluation of novel, potent, and broad

spectrum NNRTIs with antiviral activity, J. Med. Chem. 48 (2005) 7153–7165, https://doi.org/10.1021/jm050257d.
[52] S. Gemma, C. Camodeca, S. Sanna Coccone, B.P. Joshi, M. Bernetti, V. Moretti, S. Brogi, M.C.B. De Marcos, L. Savini, D. Taramelli, N. Basilico, S. Parapini, M. Rottmann, R. Brun, S. Lamponi, S. Caccia, G. Guiso, R.L. Summers, R.E. Martin, S. Saponara, B. Gorelli, E. Novellino, G. Campiani, S. Butini, Optimization of 4-aminoquinoline/clotrimazole-based hybrid antimalarials: further structure-activity relationships, in vivo studies, and preliminary toxicity profiling, J. Med. Chem. 55 (2012) 6948–6957, https://doi.org/10.1021/jm300802s.
[53] C. Lu, C. Wu, D. Ghoreishi, W. Chen, L. Wang, W. Damm, G.A. Ross, M.K. Dahlgren, E. Russell, C.D. Von Bargen, R. Abel, R.A. Friesner, E.D. Harder, OPLS4: improving force field accuracy on challenging regimes of chemical space, J Chem Theory Comput 17 (2021) 4291–4300, https://doi.org/10.1021/acs.jctc.1c00302.
[54] A. Frandsen, D.S. Pickering, B. Vestergaard, C. Kasper, B.B. Nielsen, J. R. Greenwood, G. Campiani, C. Fattorusso, M. Gajhede, A. Schousboe, J.S. Kastrup, Tyr702 is an important determinant of agonist binding and domain closure of the ligand-binding core of GluR2, Mol. Pharmacol. 67 (2005) 703–713, https://doi.org/10.1124/MOL.104.002931.
[55] Schrödinger Release 2024-2: Protein Preparation Wizard, Schrödinger, LLC, New York, NY, 2024. Epik, Schrödinger, LLC, New York, NY, 2024; Impact, Schrödinger, LLC, New York, NY; Prime.
[56] Maestro, Version 14.1, Schrödinger, LLC, New York, NY, 2024, 2024.
[57] Glide, Version 10.3, Schrödinger, LLC, New York, 2024, 2024.
[58] R.A. Friesner, J.L. Banks, R.B. Murphy, T.A. Halgren, J.J. Klicic, D.T. Mainz, M. P. Repasky, E.H. Knoll, M. Shelley, J.K. Perry, D.E. Shaw, P. Francis, P.S. Shenkin, Glide: a new approach for rapid, accurate docking and scoring. 1. Method and assessment of docking accuracy, J. Med. Chem. 47 (2004) 1739–1749, https://doi.org/10.1021/jm0306430.
[59] T.A. Halgren, R.B. Murphy, R.A. Friesner, H.S. Beard, L.L. Frye, W.T. Pollard, J. L. Banks, Glide: a new approach for rapid, accurate docking and scoring. 2. Enrichment factors in database screening, J. Med. Chem. 47 (2004) 1750–1759, https://doi.org/10.1021/jm030644s.
[60] Schrödinger Release 2024-2: MacroModel, Schrödinger, LLC, New York, NY, 2024 n.d.
[61] Schrödinger Release 2024-2: Desmond Molecular Dynamics System, D. E. Shaw Research, New York, NY, 2024, Maestro-Desmond Interoperability Tools, Schrödinger, New York, NY, 2024, 2024.
[62] L.A. Kelley, S.P. Gardner, M.J. Sutcliffe, An automated approach for clustering an ensemble of NMR-derived protein structures into conformationally related subfamilies, Protein Eng. Des. Sel. 9 (1996) 1063–1065, https://doi.org/10.1093/protein/9.11.1063.
[63] D. Remillard, D.L. Buckley, J. Paulk, G.L. Brien, M. Sonnett, H. Seo, S. Dastjerdi, M. Wühr, S. Dhe-Paganon, S.A. Armstrong, J.E. Bradner, Degradation of the BAF complex factor BRD9 by heterobifunctional ligands, Angew. Chem. Int. Ed. 56 (2017) 5738–5743, https://doi.org/10.1002/anie.201611281.
[64] G.E. Winter, D.L. Buckley, J. Paulk, J.M. Roberts, A. Souza, S. Dhe-Paganon, J. E. Bradner, Phthalimide conjugation as a strategy for in vivo target protein degradation, Science 348 (2015) 1376–1381, https://doi.org/10.1126/science.aab1433, 1979.
[65] D. Kozakov, R. Brenke, S.R. Comeau, S. Vajda, PIPER: an FFT-based protein docking program with pairwise potentials, Proteins: Struct., Funct., Bioinf. 65 (2006) 392–406, https://doi.org/10.1002/prot.21117.
[66] M.L. Drummond, C.I. Williams, *In silico* modeling of PROTAC-mediated ternary complexes: validation and application, J. Chem. Inf. Model. 59 (2019) 1634–1644, https://doi.org/10.1021/acs.jcim.8b00872.
[67] V. Ciccone, V. Simonis, C. Del Gaudio, C. Cucini, M. Ziche, L. Morbidelli, S. Donnini, ALDH1A1 confers resistance to RAF/MEK inhibitors in melanoma cells by maintaining stemness phenotype and activating PI3K/AKT signaling, Biochem. Pharmacol. 224 (2024) 116252, https://doi.org/10.1016/j.bcp.2024.116252.